nature reviews chemistry

https://doi.org/10.1038/s41570-026-00801-2

Review article

Check for updates

Understanding the degradation complexity of ultrahigh-energy lithium metal batteries

Wei Deng[1,2], Bao Qiu[1] ✉, Jiahang Chen[3], Zhen Li[3], Yongbing Tang[2] ✉, Zhaoping Liu[1] ✉ & Ying Shirley Meng[4] ✉

Abstract

The combination of Li-rich layered oxide cathodes and lithium metal anodes enables lithium metal batteries (LMBs) to achieve specific energies exceeding 600 Wh kg^{-1}, which is a crucial threshold requiring the activation of anionic oxygen-redox of cathode. The specific energy is attained owing to oxygen-redox reactions at the cathode and reversible Li plating–stripping at the anode, but these processes also induce distinct failure mechanisms. Structural destabilization at the cathode and anodic dendrite growth cause cell-level failures that impact the lifespan of LMBs more profoundly than material degradation alone. Moreover, the presence of lithium metal anodes obscures the detection of active Li loss, often leading to misinterpretations related to capacity fading and cycle life. This Review examines the progress in realizing 600 Wh kg^{-1} LMBs and understanding their lifespan failure mechanisms. We discuss the challenges in accurately assessing the lifespan and Li loss pathways of LMBs, and we elucidate the fundamental chemistry mechanisms driving both material-level and cell-level failures. In particular, the electrochemical implications of cell parameters, cell assembly and operating conditions on the lifespan are highlighted. We also outline the gaps in knowledge and advanced techniques required to decipher detailed failure modes for LMBs with oxygen-redox reactions and Li plating–stripping.

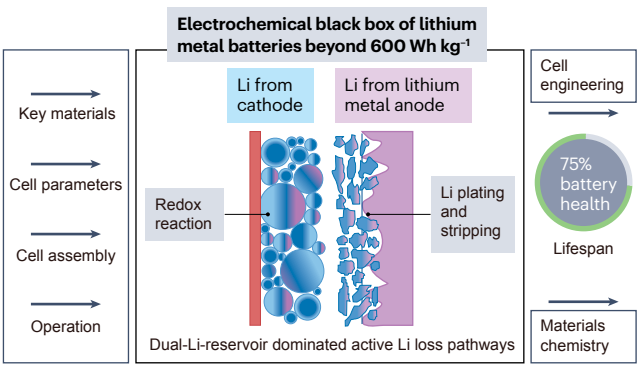

Sections

A full list of affiliations appears at the end of the paper. ✉e-mail: qiubao@nimte.ac.cn; tangyb@siat.ac.cn; liuzp@nimte.ac.cn; shirleymeng@uchicago.edu

Introduction

Lithium metal batteries (LMBs) with a specific energy exceeding 600 Wh kg^{-1} represent a crucial benchmark for next-generation batteries[1,2]. To surpass this threshold, the cells need to rely on both lithium metal anodes (LMAs) with reversible Li plating–stripping and Li-rich layered oxide (LLO) cathodes featuring oxygen-redox reactions[3,4] (Fig. 1a), which are fundamentally distinct from the chemistries in current lithium-ion batteries (LIBs). However, oxygen-redox reactions and electrochemical Li plating–stripping introduce considerable electrochemical complexity in these energy storage systems. Especially, Li plating–stripping at the anode typically leads to irreversible Li dendrite growth and dead Li proliferation, complicating the pathways of active Li loss[5]. Meanwhile, the Li-rich stoichiometry (>1.0) in LLOs induces local chemical and structural disorder in transition metal–oxygen (TM-O) polyhedra during oxygen-redox reactions[6,7]. As a result, the electrolyte must be able to tolerate strong oxidative conditions from oxygen-redox reactions[8] and the highly delithiated cathode, while remaining compatible with the interphase chemistry on both electrodes[9]. Moreover, the Coulombic efficiency (CE) for Li plating–stripping (CE_{Li}) in LMBs remains low (Fig. 1b), typically falling below 99.50% and in some cases under extreme working conditions even below 99.00%[10]. The reported maximum average CE_{Li} of ~99.90% is achievable only in coin cells under mild conditions[11,12]; however, although this value appears high, it implies a capacity decay to ~80% after just 200 cycles. Figure 1b highlights the gap between the current CE_{Li} of Ah-level LMBs and their target range of at least 99.95%, which limits their lifespan and keeps it well below the required level for 500 cycles with capacity retention of 75%.

For lifespan evaluation in LMBs, because both LLOs and LMAs serve as Li reservoirs, the active Li loss pathways differ fundamentally from those in LIBs, which contain only the single Li inventory of the cathode. Consequently, conventional lifespan evaluation metrics developed for LIBs through galvanostatic charge–discharge tests are inadequate for capturing the true reversibility of Li^+ shuttling in LMBs. As the active Li in LMA can compensate for the cathode Li loss, this process is not directly reflected in voltage-capacity curves, which is typically considered in LIBs. These distinctions are often overlooked when assessing the lifespan of LMBs. This Review aims to identify and elucidate the active Li loss pathways arising from the intrinsic dual-Li-reservoir nature of LMBs.

To achieve a specific energy of over 600 Wh kg^{-1} in LMBs, stringent control of the cell parameters is essential. Unfortunately, the impact of these parameters on battery lifespan has received limited attention. Despite broad recognition of the discrepancies in cell parameters between coin cells and Ah-level pouch cells[13,14], the reported results still exhibit substantial variability in cell engineering. In practice, cell parameters, cell assembly and operating conditions may influence lifespan more profoundly than materials innovation alone. Thus, this Review aims to spotlight the electrochemical implications of cell engineering, an often overlooked yet critical determinant of the failure modes and lifespan of LMBs. Figure 1c presents an overview of the Ah-level LMBs known to exceed 400 Wh kg^{-1}, highlighting the wide variation in both cell parameters and cycling performance. To facilitate cross-study comparisons and to more accurately reflect active Li depletion rates for different LMBs, we propose a new lifespan metric — the normalized cycle life per anode-capacity to cathode-capacity (*N*/*P*) ratio (equation 1) — which corrects for the influence of *N*/*P* ratio on absolute cycle counts:

$$Normalized\ cycle\ life = \frac{cycle\ number}{N/P\ ratio} \quad (1)$$

The top panel of Fig. 1c (400–450 Wh kg^{-1} range[15–21] and 450–500 Wh kg^{-1} range[22–24]) shows a predominance of $LiNi_aCo_bMn_{1-a-b}O_2$ (NCM, $0 < a < 1$, $0 < b < 1$) cathodes with moderate voltages (mostly in 4.2–4.3 V), *N*/*P* ratios of 1.5–2.5, and cathode areal capacity generally below 6.0 mAh cm^{-2}. Although an early study has explored LLOs, it was limited to a specific energy of 430 Wh kg^{-1} owing to low cell capacity and cathode areal capacity[25]. These studies demonstrate modest specific energy targets but still exhibit normalized cycle counts below 100 (most falling between 25 and 75), indicating limited reversibility of Li plating–stripping. In the middle panel (>500 Wh kg^{-1})[22,26–29], achieving higher specific energy requires tighter control of cell parameters, including elevated cathode areal capacity (>6.0 mAh cm^{-2})[27,28,30], higher operating voltage (up to 4.4 V, or even 4.8 V for LLOs[31]), and reduced electrolyte-to-capacity ratios (<1.5 g Ah^{-1}). More interestingly, a few studies[22,27] have taken an alternative approach by reducing areal cathode capacity and increasing stacking layers, thereby lowering the corresponding areal Li plating capacity and improving the normalized cycle count. Conversely, the bottom panel[3,32–36] of Fig. 1c shows that LMBs that reach or exceed 600 Wh kg^{-1} rely on ultrahigh areal capacity (>8.0 mAh cm^{-2})[3,36] and minimal *N*/*P* ratios (close or below 1.0)[32,35,36]. In these designs, nearly all cell parameters are pushed to their threshold of practical feasibility, a delicate balance that is well-illustrated by the *N*/*P* ratio. Although this ratio is often minimized to reduce anode mass and maximize specific energy, excessive reduction inevitably compromises cycle life owing to insufficient Li inventory. To construct a 600 Wh kg^{-1} cell, it is necessary to increase the specific discharge capacity and areal loading of the cathode. However, high areal loading introduces diminishing returns, which means that the gain in cell-level specific energy saturates beyond a certain threshold. Thus, reducing the mass of the anode, electrolyte and separator is a critical strategy to controlling the overall cell mass. Evidently, the higher cathode areal capacity and the lower anode mass concurrently result in *N*/*P* ratios below 1.0. However, careful cell design can mitigate an excessively low *N*/*P* ratio, and doing so often increases the performance pressure on other materials and design parameters. As a result, most of these cells deliver normalized cycle counts less than 75, with 700 Wh kg^{-1} prototype cells lasting just a few cycles[36]. Thus, achieving over 600 Wh kg^{-1} in LMBs requires far more than simply scaling the size of existing 500 Wh kg^{-1}

Fig. 1 | Research status of Ah-level LMBs. a, LMBs designed to exceed 600 Wh kg^{-1}, highlighting the distinct contributions of the oxygen-redox reaction and Li plating–stripping process. **b**, Correlation between cell-level specific energies and Coulombic efficiencies (CEs) in lithium-ion batteries (LIBs), and reported Coulombic efficiencies for Li plating–stripping (CE_{Li}, from coin or pouch cells) and specific energies in Ah-level LMBs. The LFP, Gr and Si-Gr means lithium iron phosphate cathode, graphite anode and silicon–graphite anode, respectively. **c**, Summary of the reported Ah-level LMBs with specific energies >400 Wh kg^{-1}, highlighting key cell parameters and their corresponding normalized cycle counts per anode-capacity to cathode-capacity (*N*/*P*) ratio. Four cell parameters (cell capacity, cathode type, working voltage of cathode, and cathode areal capacity) are positioned to the left of normalized cycle count, as they have crucial roles in determining specific energy. The *N*/*P* ratio and electrolyte-to-capacity (*E*/*C*) ratio (g Ah^{-1}) positioned to the right are typically tuned to meet minimum threshold for achieving targeted specific energies during cell designs, yet they critically influence the usable lifespan of LMBs. NCM refers to $LiNi_aCo_bMn_{1-a-b}O_2$ ($0 < a < 1$, $0 < b < 1$) cathode material. LLO, Li-rich layered oxide.

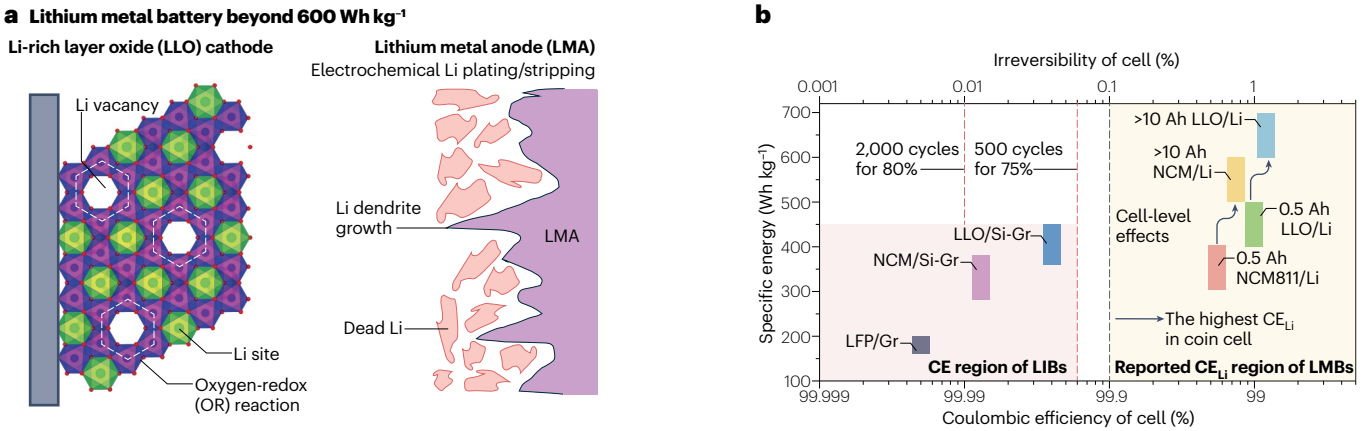
a Lithium metal battery beyond 600 Wh kg⁻¹
Li-rich layer oxide (LLO) cathode
Lithium metal anode (LMA)
Electrochemical Li plating/stripping
Li vacancy
Li site
Oxygen-redox (OR) reaction
Li dendrite growth
LMA
Dead Li
b
Irreversibility of cell (%)
0.001
0.01
0.1
1
Specific energy (Wh kg⁻¹)
700
600
500
400
300
200
100
2,000 cycles for 80%
500 cycles for 75%
>10 Ah LLO/Li
>10 Ah NCM/Li
Cell-level effects
0.5 Ah LLO/Li
0.5 Ah NCM811/Li
LLO/Si-Gr
NCM/Si-Gr
LFP/Gr
The highest CE_Li in coin cell
CE region of LIBs
Reported CE_Li region of LMBs
99.999
99.99
99.9
99
Coulombic efficiency of cell (%)

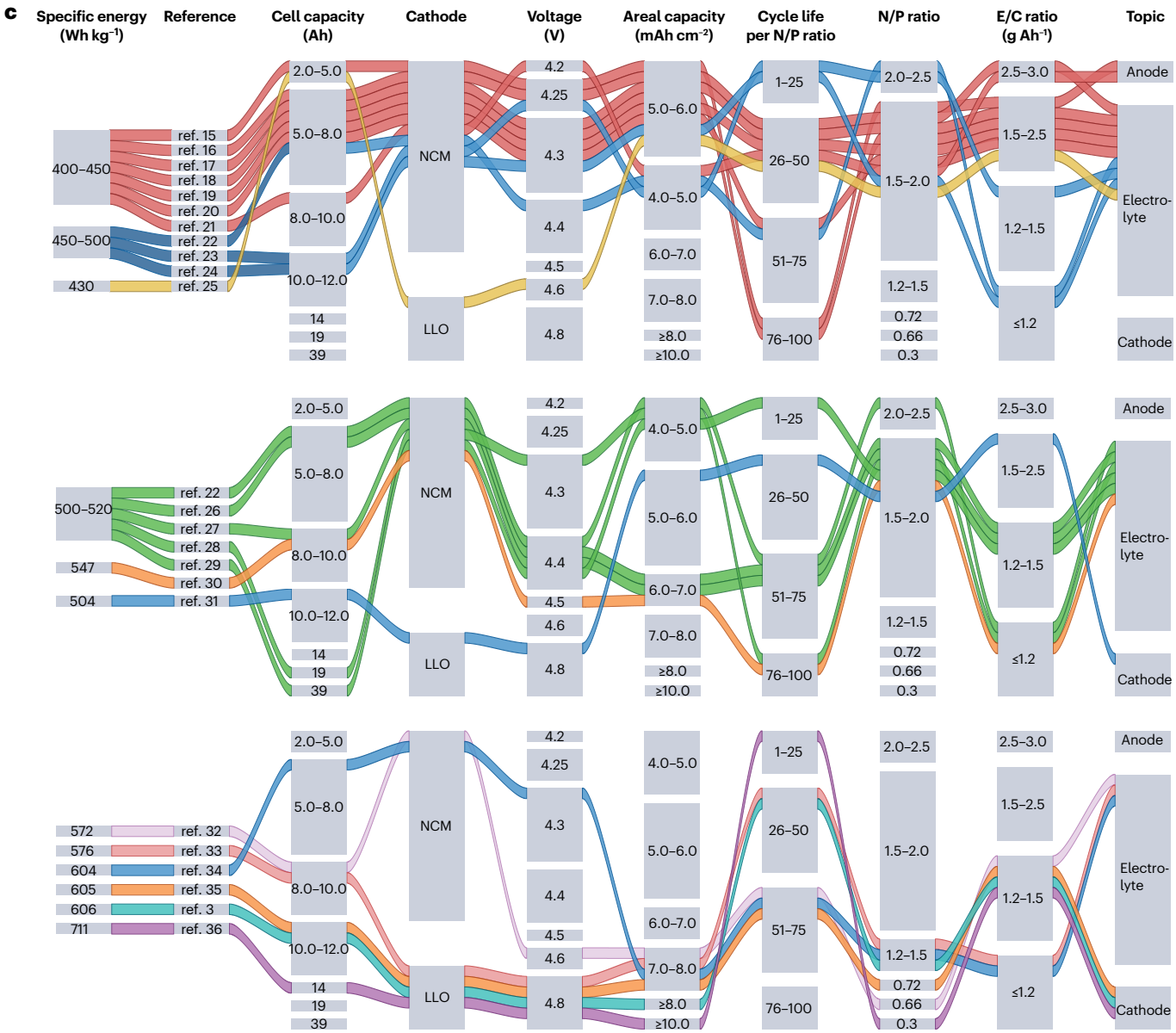
c
Specific energy (Wh kg⁻¹)
Reference
Cell capacity (Ah)
Cathode
Voltage (V)
Areal capacity (mAh cm⁻²)
Cycle life per N/P ratio
N/P ratio
E/C ratio (g Ah⁻¹)
Topic
400–450
450–500
430
ref. 15
ref. 16
ref. 17
ref. 18
ref. 19
ref. 20
ref. 21
ref. 22
ref. 23
ref. 24
ref. 25
2.0–5.0
5.0–8.0
8.0–10.0
10.0–12.0
14
19
39
NCM
LLO
4.2
4.25
4.3
4.4
4.5
4.6
4.8
5.0–6.0
4.0–5.0
6.0–7.0
7.0–8.0
≥8.0
≥10.0
1–25
26–50
51–75
76–100
2.0–2.5
1.5–2.0
1.2–1.5
0.72
0.66
0.3
2.5–3.0
1.5–2.5
1.2–1.5
≤1.2
Anode
Electro-lyte
Cathode
500–520
547
504
ref. 22
ref. 26
ref. 27
ref. 28
ref. 29
ref. 30
ref. 31
572
576
604
605
606
711
ref. 32
ref. 33
ref. 34
ref. 35
ref. 3
ref. 36

cell designs. The key challenges involve developing cathodes with high specific discharge capacity and high average working voltage to increase the specific energy of a cell, as well as formulating electrolytes that are compatible with both the anode and cathode. Furthermore, it is critical to slow the consumption rate of active Li under high-areal-capacity conditions. Finally, complex trade-offs between specific energy, lifespan, fundamental material limits, aggressive design parameters and practical manufacturing processes must be carefully managed, often at the expense of lifespan[37].

In this Review, we outline the characteristic features of the distinct failure stages in LMBs by elucidating the active Li loss pathways. We then analyse both material-level and cell-level degradation mechanisms driven by oxygen-redox reactions and Li plating–stripping. The electrochemical implications of cell parameters, cell assembly and operating conditions on LMB lifespan are then discussed in detail. Finally, we identify the gaps in knowledge and highlight the need for advanced diagnostic techniques to clarify the failure mechanisms affecting the lifespan of LMBs.

Lifespan failure stages

The failure stages of LMBs are governed by the dynamics of active Li loss during cycling. In LIBs, wherein the cathode is the sole Li reservoir, any irreversible Li loss (depicted in Fig. 2a as white regions in the cathode after cycling) corresponds to the Li^+ that fails to return to the cathode following intercalation of the graphite anode. Inactive Li forms electrode interphases, becomes trapped in and is irreversibly plated on the graphite anode. Thus, the CE of a cell (CE_{cell}) in LIBs, determined by the electrode (anode or cathode) with the lowest CE, quantifies the per-cycle loss of active Li. In anode-free LMBs (AFLMB, Fig. 2b) — in addition to

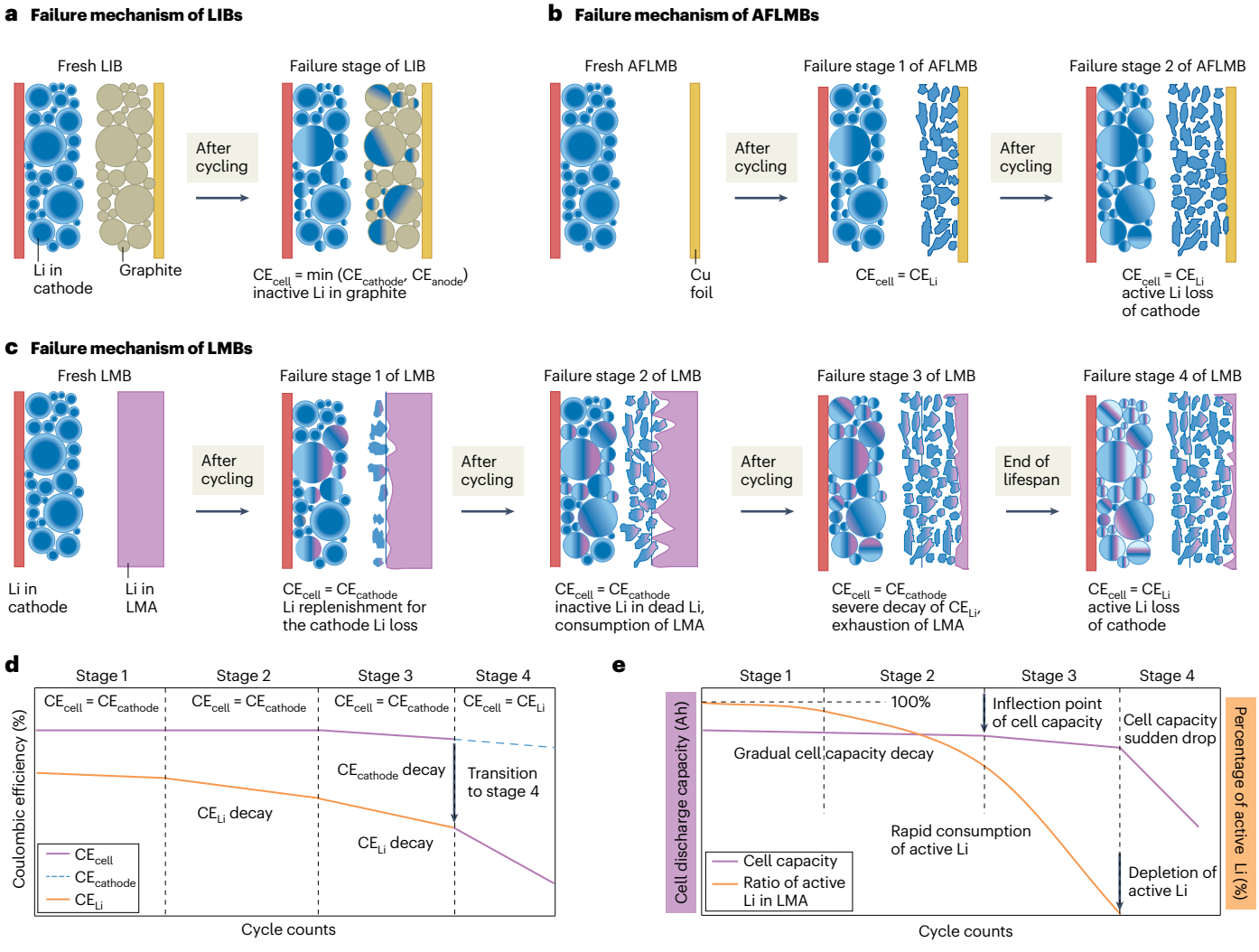

Fig. 2 | Lifespan failure stages of LMBs. The distinct failure mechanisms and active Li loss pathways in lithium-ion batteries (LIBs) (part **a**), anode-free lithium metal batteries (AFLMBs) (part **b**) and LMBs (part **c**). To clearly depict Li loss pathways, Li originating from the cathode and lithium metal anode (LMA) are marked in blue and pale purple, respectively. White regions within cathode particles indicate active Li loss from the cathode, whereas the pale purple area of the cathode in part **c** shows the Li replenished from the LMA. Dead Li particles are shown in both blue and pale purple, corresponding to their origins from both the cathode and LMA. Part **d** presents variations of Coulombic efficiencies for Li plating–stripping (CE_{Li}), Coulombic efficiencies of cell (CE_{cell}), and Coulombic efficiencies of cathode ($CE_{cathode}$), whereas part **e** presents the corresponding changes in cell capacity and the proportion of active Li remaining in the LMA during different failure stages, revealing the presence of invisible active Li loss underlying the gradual capacity decay.

interphase-trapped Li — the electrochemical Li plating–stripping cycle produces dead Li, which consumes the Li in the cathode. However, given that capacity retention scales exponentially with cycle number in AFLMBs, typical CE_{Li} values falling below 99.50% (wherein $0.995^{200} \approx 37\%$ retention)[10] are insufficient for long-term cycling and remain lower than normal CE of the cathode ($CE_{cathode}$) of ~99.98% (wherein $0.9998^{200} \approx 96\%$ retention). Consequently, the CE_{cell} of AFLMBs essentially represents CE_{Li} according to galvanostatic charge–discharge results. In LMBs (Fig. 2c), however, LMAs act as excess Li reservoirs that can compensate for the Li loss of the anode during plating–stripping. This can lead to misinterpreted galvanostatic charge–discharge experimental results indicating that 100% of the Li extracted from the cathode is returned to the cathode. For this reason, symmetric Li cells should be avoided when assessing the reversibility of Li plating–stripping owing to their vulnerability to soft-shorts (small localized electrical connection between two electrodes)[38] and dual-Li-reservoir character; instead, AFLMBs are strongly suggested when investigating CEs. Before the Li reservoir is depleted in the LMBs, the CE_{cell} mainly reflects $CE_{cathode}$ owing to the Li compensation mechanism of the Li-contained anode. However, once the reservoir is exhausted, the previously masked irreversible Li loss during plating–stripping emerges, shifting the governing factor of the CE_{cell} from $CE_{cathode}$ to CE_{Li}. Therefore, cell capacity decay alone does not reliably indicate the degradation of LMBs, as it fails to account for the progressive depletion of LMA. Importantly, the accumulation of inactive Li at the electrode interface during cycling compromises the reversibility of subsequent Li plating–stripping, inducing a self-accelerating degradation mechanism. Thus, the depletion rate of the Li reservoir is governed by CE_{Li} and follows an exponential rather than linear trajectory[39].

The invisible failure of LMAs in electrochemical tests, characterized by the absence of distinct signatures in routine charge–discharge curves, presents considerable challenges in identifying the failure stages of LMBs. To illustrate Li loss pathways and their origins, Fig. 2c marks the different Li sources (anode and cathode) with distinct colours. Initially, the battery operates with stable CE_{Li} and $CE_{cathode}$ (Fig. 2d, stage 1). However, irreversible Li plating–stripping results in the continuous Li loss of the cathode, which is then replenished by the Li inventory in the LMA. At this stage, inactive Li in the newly formed dead Li is mainly found from the cathode. Although the cell capacity remains stable (Fig. 2e, stage 1), the repeated replenishment for the cathode consumes the bulk LMA and induces surface roughening[40]. As cycling continues, surface pits and morphological irregularities on the LMA — coupled with the accumulation of dead Li, which disrupts interfacial Li^+ distribution homogeneity[41] — promote uneven Li plating and dendrite growth. In stage 2, the CE_{Li} begins to decline gradually, whereas $CE_{cathode}$ remains stable. The cell capacity still appears stable owing to ongoing Li compensation; however, the rate of Li loss in the LMA accelerates. This leads to increased polarization, interfacial instability and cell swelling. Particularly for LLOs with voltage decay characteristics, tracking energy degradation instead of capacity alone provides better insight into the rising impedance and declining kinetics. Notably for LLOs, the inflexion points in energy curves of electrochemical performances can help distinguish stage 2 from stage 1. The trends in cell capacity and active Li consumption during stage 1 and 2 are supported by quantitative analysis, which indicates the differences of Li loss in pouch cells under varying stack pressures[39], despite showing similar capacity retention.

The decay of CE_{Li} in stages 1 and 2 initiates a cascade of degradation. The growth of a porous, insulating dead Li layer increases both ohmic impedance and concentration polarization, which causes further capacity fading[42]. The increased impedance also generates increased temperatures during charging–discharging processes, destabilizing the cathode–electrolyte interface. Furthermore, surface roughening accelerates localized cell expansion, disrupting multi-physics uniformity and concentrating current density. The current concentration forces a greater delithiation depth in the respective regions of the cathode, inducing local crack formation. Thus, by stage 3, the cumulative impact of these factors causes the intrinsic capacity of the cathode and the reversibility of Li^+ intercalation to decay, which manifests as an inflection point wherein capacity fade accelerates considerably. As the irreversibility of Li plating–stripping deteriorates exponentially[39], the degradation of both cathode and CE_{Li} rapidly depletes the residual LMA. This critical failure state, wherein the anode is nearly exhausted, is often masked by the gradual capacity decay observed in standard galvanostatic tests. The ratio of the cycle count at the end of stage 3 to the *N*/*P* ratio could be considered as the proposed normalized cycle life. Stage 4 begins once the LMA is fully depleted; thus, it is evident that cells with lower *N*/*P* ratios reach this stage earlier. Without the ability to compensate for the loss of Li at the cathode, Li plating–stripping becomes the dominant contributor to irreversible Li loss, and the CE_{cell} is entirely governed by CE_{Li} marked by a step-like drop in CE_{cell}. From this stage, the battery exhibits failure characteristics similar to those of AFLMBs, with rapid capacity decline marking end-of-life[43]. However, despite the diagnosis of such transitions, published works often emphasize stable cycling performance, while neglecting to report the inflection points in the CE_{cell} and capacity that clearly indicate the onset of battery failure. It is important to recognize that this four-stage model is an idealized framework based on the evolution of CEs, intended to connect internal degradation metrics (CE_{Li} and active Li loss) with external electrochemical performance. In practice, the failure process of a cell rarely presents this perfectly, and any analysis must be grounded in the specific electrochemical data and a direct failure analysis.

Lifespan failure chemistry

This section aims to provide a systematic breakdown of the intricate trade-offs linking cell design, energy density and cycle life. The discussion is structured around four critical perspectives: key materials, cell parameters, cell engineering and operating conditions.

Chemistry of materials

Figure 3 highlights how oxygen-redox reactions and electrochemical Li plating–stripping contribute to the depletion of the active Li inventory in LMAs and highlights the associated cell-level failures. Deintercalation of Li^+ from LLOs triggers oxygen-redox reactions, inducing O–O dimer and molecular O_2 formation that weaken the TM-O lattice interactions and lead to the collapse of TM-O polyhedra[44,45] (**1** in Fig. 3). Particularly at the cathode surface, the greater degree of delithiation relative to the bulk induces severe collapse and surface oxygen loss, increasing Li^+ intercalation resistance. To minimize the energy level of the lattice during discharging, the formation of molecular O_2 causes surface TM ions to migrate into Li layer (**2** in Fig. 3), which forms a spinel-like phase that contributes to the large initial capacity loss[45–47] and poor rate capability[48]. During cycling, continuous distortion of TM-O polyhedra (**3** in Fig. 3) modifies the local electronic structure of the TM and oxygen, shifting the redox potential and driving the characteristic voltage decay in LLOs[49–51]. To stabilize the TM-O polyhedra, introducing pillar ions (such as, Mg^{2+}, Na^+, K^+ and Al^{3+}) into the Li slab reinforces the layered structure[52–54], whereas doping La^{3+}, Ce^{4+} and Nb^{5+} at TM sites can suppress Li/TM mixing by maintaining specific oxidation states[55–57] or by spatially hindering TM migration (with B^{3+}, F^- or Cl^-)[58–60]. Furthermore, voltage decay could be alleviated by substituting TMs with Zr^{4+} and Al^{3+} (refs. 61,62), and lattice oxygen can be stabilized by

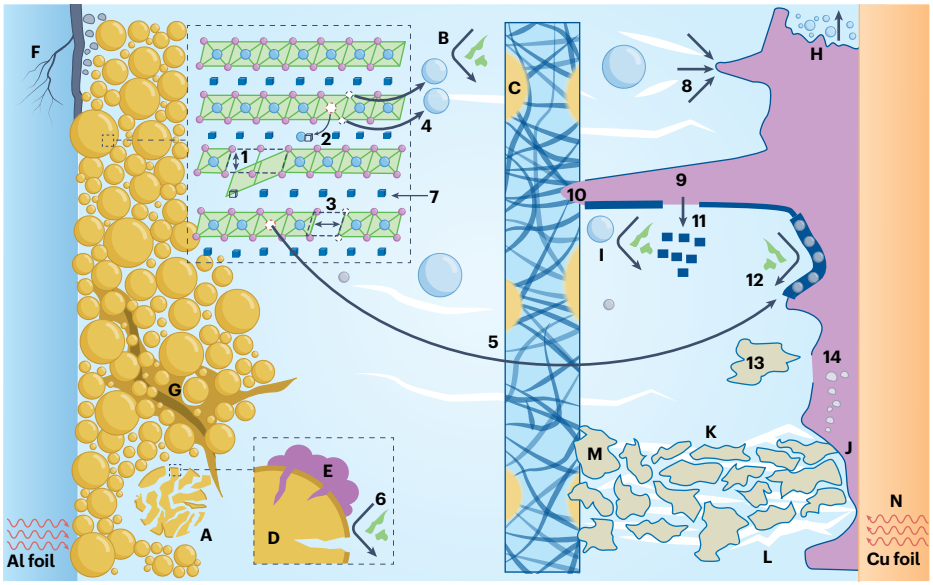

Fig. 3 | Material-level degradation aspects (labelled 1–14) and corresponding cell-level impacts (labelled A–N) of the lifespan failure of lithium metal batteries. To differentiate the origins of various failure aspects from oxygen-redox reactions and Li plating–stripping processes, light pink, pale yellow, green and blue colours are used to represent failures related to the cathode, lithium metal anode (LMA), electrolyte and separator, respectively. White regions in the illustration represent areas of local electrolyte depletion. SEI, solid electrolyte interphase; TM, transition metal; TM-O, transition metal–oxygen.

Cathode
Anode
Electrolyte
Separator

Cathode particle
Dead Li particle
Oxygen
Electrolyte breakdown

Material-level degradation (1–14)	Cell-level degradation (A–N)
1 Collapse of TM-O polyhedra	**A** Cathode particle pulverization
2 Surface TM ion migration to Li sites	**B** Oxygen-induced electrolyte decomposition
3 Distortion of TM-O polyhedra	**C** By-products blocking separator porosity
4 Instability of lattice oxygen	**D** Surface-localized cracking of cathode
5 TM ion dissolution and migration to anode	**E** Cathode interfacial by-products
6 Electrolyte oxidation at cathode surface	**F** Localized foil corrosion and cracking
7 Increasing Li ion transfer resistance	**G** Electrode without conductive contact
8 Local ion depletion and charge accumulation	**H** Galvanic corrosion of LMA
9 Li dendrite growth	**I** Chemical corrosion of LMA
10 Penetration and rupture of SEI	**J** Exhaustion of active Li in bulk LMA
11 SEI dissolution and decomposition	**K** Accumulation of porous dead Li layer
12 Electrolyte reduction at metallic Li	**L** Localized insufficient electrolyte wettability
13 Root-preferred stripping to form dead Li	**M** Dead Li blocking separator surface
14 Multi-site cavitation on bulk LMA	**N** Uneven Joule heat distribution

incorporating strongly bonded dopants, such as Ti^{4+}, Ta^{5+}, V^{5+}, W^{6+} and Mo^{6+} (refs. 63–67). Nevertheless, in LLO calcination engineering, the foremost task is to stabilize the lattice through doping without compromising the specific capacity.

Once lattice distortion occurs, it induces grain-level anisotropic stress, causing uneven volume changes and strain across grain boundaries. Intragranular cracks can then form and propagate along crystallographic *a*–*b* planes, with their formation influenced by the delithiation degree, leading to cathode particle pulverization[68] (**A** in Fig. 3). To counteract this, high densities of precipitates with lattice mismatch have been reported to dissipate internal strain by manipulating the crystallographic orientation of planes[69,70], such as with radially aligned primary particles oriented along the [001] plane in LLOs[71]. Another result of lattice distortion is the instability of lattice oxygen (**4** in Fig. 3), which arise from the formation of oxygen vacancies[72,73]. This instability facilitates the release of reactive oxygen species in the form of radicals ($O\cdot$ or $O^{\cdot 2-}$) and singlet oxygen ($^1O_2$)[74]. These oxygen species drive the consumption of solvents, lithium salts and additives in the bulk electrolyte (**B** in Fig. 3), generating by-products that block separator pores (**C** in Fig. 3) and hinder ion diffusion. Moreover, oxygen release destabilizes the TM-O polyhedra in near-surface region of LLOs, initiating TM dissolution into electrolyte and subsequent migration towards the anode[75] (**5** in Fig. 3). The combined effects of chemical oxidation from highly delithiated LLOs, electrochemical oxidation under high potentials, and surface-localized cracking of the cathode (**D** in Fig. 3) induced by oxygen release collectively intensify the electrolyte decomposition and cathode surface degradation at the cathode–electrolyte

interface (**6** in Fig. 3). The surface instability is further exacerbated by the polycrystalline nature of LLOs, promoting intergranular crack formation between the primary particles[76]. Consequently, cathode interfacial by-products (**E** in Fig. 3) can largely increase the resistance related to interfacial Li^+ transfer (**7** in Fig. 3). To address the surface oxygen instability and suppress interfacial reactivity, typical strategies include surface gradient doping[77], the introduction of surface oxygen vacancies[78], and conformal coating such as atomic layer deposition[79]. Additionally, the residual TM impurities and hydroxyl groups on conductive carbon additives catalyse electrolyte decomposition[80], whereas mechanical strain from cathode pulverization imposes localized foil corrosion and cracking (**F** in Fig. 3), leading to insufficient conductive contact (**G** in Fig. 3) between cathode particles and the foil.

Once Li^+ reaches the anode interface during charging, it is reduced to metallic Li, which aggregate to form initial Li clusters that act as seeds for further electroplating, determining the morphology and CE_{Li}. To prevent local aggregation of Li atoms, regulating the atomic packing density and crystallographic orientation in Li alloys (such as, Li_9Al_4–LiMg (ref. 81), Li–Mg (ref. 82) and Li–Al (ref. 83)) can enhance the in-plane ion diffusion. Notably, reactive molecular dynamics simulations reveal that Li atoms tend to undergo a disorder-to-order transition once the aggregated cluster exceeds a critical size around 5–8 nm. Thus, enhancing surface diffusion to inhibit the formation of large, ordered clusters, and instead promoting amorphous or glassy Li nuclei, free of organized nanostructures and grain boundaries, can improve the reversibility of Li plating–stripping[84]. Thermodynamically, the heterogeneous nucleation process in electroplating is governed by the energy barrier required to form critical Li nuclei. It is widely accepted that the lithiophilic interface and a low current density can reduce the nucleation barrier of Li and improve CE_{Li} by enabling the formation of larger and less compact Li nuclei[85,86]. That is why increasing the surface area of LMAs or current collectors, which reduces the local current density and nucleation overpotential, has been shown to improve CE_{Li}[87]. However, Li plating morphology is not solely determined by current density. Rather, it is governed by the mismatch between ion diffusion and charge transfer, as described by space charge theory[88], which elucidates the local electric fields induced by ion depletion, and Sand's time model[89], which predicts the critical onset of dendrite growth. When charge transfer kinetics surpass Li^+ diffusion, local ion depletion (**8** in Fig. 3) near anode–electrolyte interfaces induce electric field inhomogeneities that direct the Li^+ flux towards specific sites, initiating the formation of local protrusions. These high-curvature protrusions or kinks intensify local charge accumulation (**8** in Fig. 3) and Li^+ consumption[90], accelerating the growth of whisker, mossy or dendritic morphologies, collectively termed Li dendrites[89] (**9** in Fig. 3). Thus, reported strategies to suppress Li dendrite growth aim to eliminate this mismatch, including the design of mixed ion and electron conductive scaffolds[91], the construction of interphases with rapid Li-ion transport ability[92], and the use of high-concentration or high-conductivity electrolytes.

One consequence of Li dendrite growth is the localized volume expansion beneath the solid electrolyte interphase (SEI), which penetrates, destabilizes and ruptures the SEI (**10** in Fig. 3), contributing to the poor reversibility of Li plating–stripping. After SEI rupture, the subsequent exposure of fresh Li to the electrolyte triggers parasitic interfacial reactions, active Li loss and SEI thickening, whereas repeated rupture and exposure sustain a cycle of interfacial degradation. Minimizing Li dendrite penetration through the interphase (or SEI) is crucial. Most studies focus on constructing interphase with high Young's modulus, as the metallic Li dendrites with plastic deformability can be mechanically suppressed when the interphase is stiffer than Li (ref. 93). Alternatively, work has also proposed mechanically flexible (rather than brittle) interphase that accommodate dendrite-induced volume expansion[94]. Another strategy to address SEI rupture-induced failure is to reduce the chemical reactivity between the anode and electrolyte, such as by using Li–In alloys[95]. Beyond the mechanical degradation of an interphase, the solubility of SEI components (**11** in Fig. 3) in non-aqueous electrolytes[96] further initiates galvanic corrosion (**H** in Fig. 3) and chemical corrosion (**I** in Fig. 3) of metallic Li. Galvanic corrosion, a failure mode unique to LMBs, driven by the potential differences between LMA and Cu (or current collector), accelerates Li oxidation through the Kirkendall effect (interfacial void formation driven by distinct diffusion rates) to deplete the Li inventory[97]. Conversely, chemical corrosion involves electron transfer from Li to solvents and lithium salts, resulting in their reduction (**12** in Fig. 3) and active Li loss in bulk LMA. A quantitative study has shown that the consumption of lithium salts is a important contributor to the lifespan failure of LMBs[98]. Additionally, crosstalk of cathode failure further destabilizes the SEI, as dissolved TM ions (such as, Mn^{2+}) deposit on the SEI of LMA[99], disrupting its integrity and ionic transport. These TM species not only enhances electron tunnelling for serious electrolyte breakdown[100] but also induces the ion-exchange reactions in SEI that seriously impair Li^+ mobility[101].

Another consequence of Li dendrite growth is base-preferred stripping, wherein Li is stripped from the root of the dendrite, rather than from the inward electrolyte interface. This leaves electrically isolated tips as dead Li (**13** in Fig. 3), which is a major contributor for Li inventory depletion[102]. Furthermore, local effects are particularly pronounced at the kinks of Li dendrites[103], wherein heterogeneous SEIs and stress fields also cause local Li stripping to initiate the formation of isolated dead Li. An in situ transmission electron microscope (TEM) study has revealed that the ratio of SEI thickness to dendrite radius determines the stripping modes, wherein SEI buckling and compression induce multi-site cavitation on LMA[104] (**14** in Fig. 3). Similarly, operando optical microscopy shows dendrite shrinking until they become electrically isolated[105], after which stripping proceeds from the bulk LMA base to supply Li for cathode intercalation during discharging. The continuous stripping leads to pit formation and growth on the LMA base and further consumes the active Li in the bulk LMA[40] (**J** in Fig. 3). During cycling, these dead Li particles accumulate at rough and irregular interface sites to form a porous dead Li layer (**K** in Fig. 3) under the constraint of stack pressure. The formation of a porous, electrically insulating dead Li layer increases the anode thickness, contributing to cell swelling and impeding ion or charge distribution[106], thereby elevating both ohmic and concentration polarization. For example, a 2.0 Ah Li/NCM (350 Wh kg^{-1}) cell was shown to experience single-layer LMA expansion from 20 µm to 70 µm after 600 cycles[107]. Dead Li accumulation, thus, becomes the most critical cell-level manifestation of irreversible Li plating–stripping, underlying most late-stage failures. For example, electrolyte consumption caused by dendrite growth and parasitic reactions at both electrodes reduce the local wettability (**L** in Fig. 3) of porous dead Li layers to worsen the concentration polarization[41,107]. Moreover, when the dead Li layer makes contacts with the separator, it undergoes plastic deformation to block the surface of the separator (**M** in Fig. 3), hindering local Li^+ transport. These effects drive cell impedance rise and intensify localized Joule heat accumulation (**N** in Fig. 3) during charging–discharging, which in turn accelerates temperature-induced cell degradation. Although suppressing Li dendrite growth remains the primary way to address dead Li layer concerns, alternative approaches such as rejuvenating dead Li through redox chemistry and electrochemical protocols have also shown promise in practical applications[102].

Electrochemical implications of cell parameters

Cell parameters must be pushed to the limits of extreme cell design, fabrication boundaries and safe operating threshold to minimize the proportion of inactive components and achieve specific energy exceeding 600 Wh kg^{-1}. However, such aggressive designs inevitably exacerbate degradation processes, in many cases imposing more detrimental impacts on battery lifespan than material-level optimization alone. Figure 4 summarizes how extreme cell parameters influence the degradation pathways, including oxygen-redox reactions, electrochemical Li plating–stripping processes, material failure modes and electrochemical instabilities.

High cathode areal loading is often prioritized for its direct contribution to specific energy. However, thick electrodes create considerable

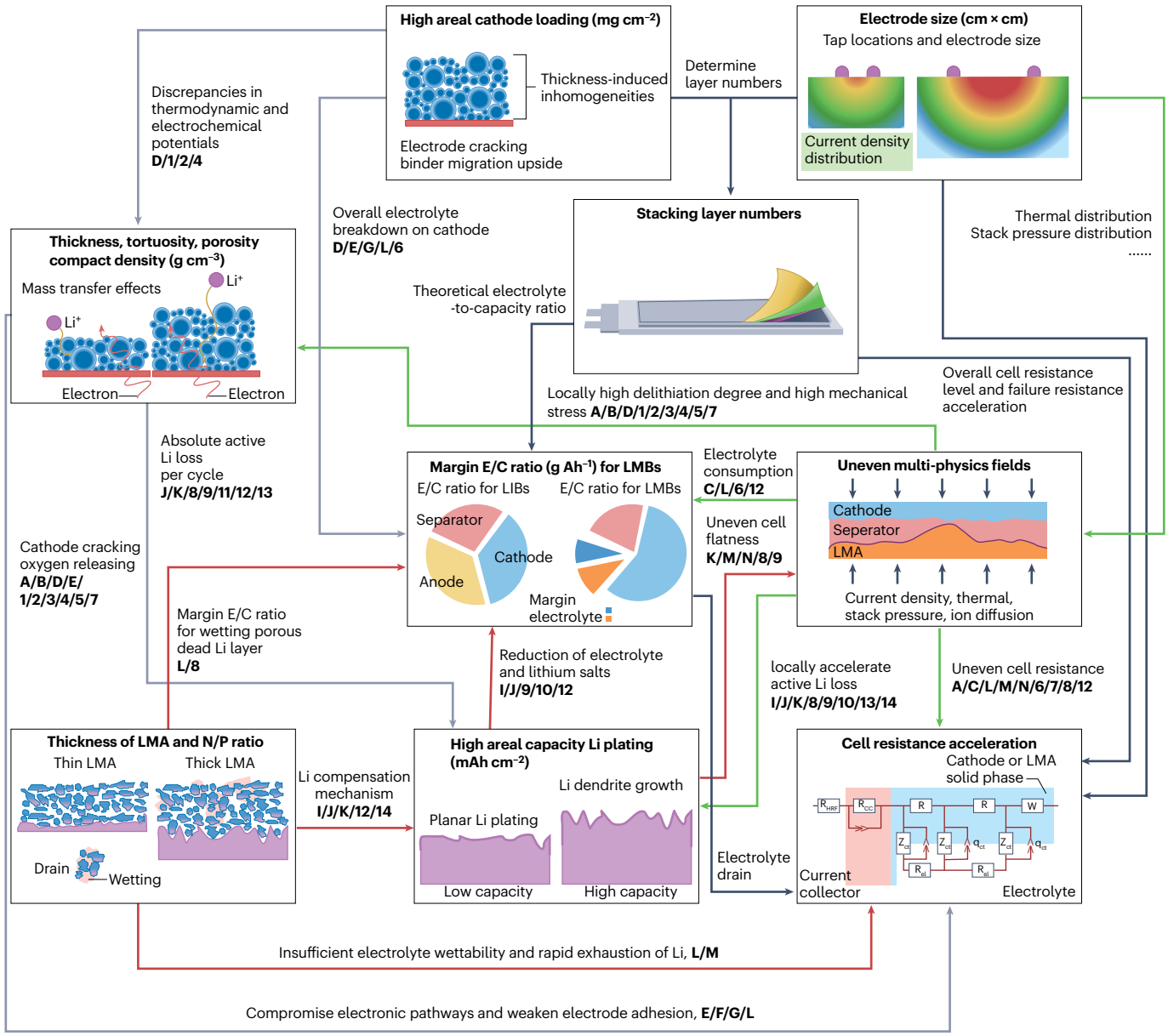

Fig. 4 | The electrochemical implications of cell parameters on lifespan failure of LMBs. The schematic illustrates how the key cell parameters are determined by the targeted specific energy of LMBs, and it highlights their interrelationships with material degradation and cell failure mechanisms. The cell parameters analysed here include areal cathode loading, cathode compacted density, electrode dimensions, stacking layer numbers, electrolyte-to-capacity (*E*/*C*) ratios, anode-capacity to cathode-capacity (*N*/*P*) ratios, thickness of lithium metal anode (LMA), and resistance levels. Coloured arrows represent four degradation-driving factors: grey arrows highlight cathode-related parameters and the impact of oxygen-redox reaction, green arrows denote the influence of electrode size on multi-physics distributions, navy arrows indicate the impact of stacking layers on overall cell resistance, and red arrows reflect degradation originating from Li plating–stripping. Degradation aspects (labelled 1–14 and A–N in Fig. 3) associated with these parameters are annotated along the corresponding arrows. In practical cell design, adjusting any single parameter not only impacts the specific energies and degradation pathways but also requires compensatory changes in other parameters to maintain a balance between specific energies and lifespan.

transport limitations for both ions and electrons. Cathode particles near the separator have access to ions from the electrolyte but may be electronically limited, whereas particles near the current collector are electronically well-connected but starved of ions that must traverse a long and tortuous diffusion path. These opposing limitations aggravate spatial discrepancies in thermodynamic and electrochemical potentials (**D**, **1**, **2** and **4** in Figs. 3 and 4), resulting in heterogeneous delithiation rates across the electrode depth[108]. The complexity of porous electrode structures under high mass loading, characterized by poor electrolyte wettability, highly compacted cathode with increased density, high tortuosity and compromised ionic and electronic pathways, substantially hinders efficient Li^+ intercalation–deintercalation and limit cathode capacity utilization[3,35]. For instance, highly compacted, increased-density thick polycrystalline LLO electrodes induces stress gradients and possible cracks in primary particles, prompting surface oxygen release and electrolyte decomposition (**A**, **B**, **D**, **E**, **1**, **2**, **3**, **4**, **5** and **7** in Figs. 3 and 4). Thick electrodes are susceptible to multiple fabrication-induced defects, including the cracking of electrode coatings, particle fracture under high compacted density, binder migration and inhomogeneous distribution of conductive additives during slurry casting and drying[109], which compromise electronic pathways and impair the interfacial adhesion between the electrode coating and the current collector (**E**, **F**, **G** and **L** in Figs. 3 and 4).

High-areal-capacity Li plating arising from high cathode loading continuously consumes and easily depletes the interfacial Li^+ at anode interfaces, which initiate subsequent Li dendrite growth. Accordingly, high-areal-capacity Li plating capacity inevitably reduces CE_{Li}. Lower CE_{Li} accelerates the absolute Li loss per charge–discharge cycle (**J**, **K**, **8**, **9**, **11**, **12** and **13** in Figs. 3 and 4) under high-areal-capacity condition, rapidly depleting the LMA and forming porous dead Li layers[110]. Meanwhile, repeated SEI rupture continuously drives the reduction of electrolyte solvents and lithium salts (**I**, **J**, **9**, **10** and **12** in Figs. 3 and 4). As discussed above, a higher *N*/*P* ratio can offset the absolute Li loss per cycle, thereby delaying the depletion of the LMA (**I**, **J**, **K**, **12** and **14** in Figs. 3 and 4) and postponing the transition to failure stage 4. However, high *N*/*P* ratio (that is, thicker LMA) is not universally beneficial. Although it delays Li exhaustion, it also permits a greater amount of inactive Li, which accumulates as thicker dead Li layers. This aggregation introduces additional voids that reduce surface wettability and hinder the electrochemical reactivation of dead Li. In such cases, effective electrolyte wetting is essential to avoid localized concentration polarization (**L** and **M** in Figs. 3 and 4) and prevent rapid capacity decay. By contrast, thinner LMA effectively suppresses dead Li build-up and electrolyte infiltration-induced failure, but the LMA are also more vulnerable to rapid depletion owing to their lower *N*/*P* ratios. For instance, a 50-μm LMA exhibited a shorter cycle life of 450 cycles compared to 600 cycles for a 20-μm LMA under identical conditions[107]. Beyond the theoretical electrolyte-to-capacity ratio required for wetting cathodes and separators, future cell designs should include electrolyte injection margins accounting for their decomposition on LLO cathodes (**D**, **E**, **G**, **L and 6** in Figs. 3 and 4) and dynamic wettability demands for dead Li layers (**L** and **8** in Figs. 3 and 4), which must be carefully balanced against the specific energy to maintain effective wetting and minimize concentration polarization.

Electrode dimensions represent another critical parameter for achieving high specific energy. Evidently, larger electrodes help to increase specific energy. Meanwhile, scaling up electrode size reduces stacking layers to decrease overall cell impedance, which diminishes Joule heating and thermal-induced degradation during cycling. However, increasing electrode size does not always yield proportional gains; beyond a certain threshold, it exhibits diminishing returns in boosting specific energy and instead compromise the uniformity of internal electrochemical reaction. Large electrode sizes amplify current and voltage non-uniformities in two-tab electrode configurations, typically exhibiting concentrated current density near the tab regions, whereas electrode edges and corners experience relatively lower currents. These disparities generate inherent electrochemical field gradients that[111], through cycling, trigger secondary multi-physics inhomogeneities, such as heating, mechanical stress, pressure, cell swelling, and polarizations. Large electrodes are more prone to misalignment of overhangs during Z-stacking or lamination stacking, which can trigger irreversible Li plating at the overhang regions to lose the active Li inventory. Consequently, larger electrode dimensions can amplify in-plane heterogeneity in electrochemical kinetics, which impacts the failure process of cathode and anode. On the cathode side, this heterogeneity can induce localized regions of high delithiation, promoting the collapse of the crystal structure and accelerating particle cracking (**A**, **B**, **D**, **1**, **2**, **3**, **4**, **5** and **7** in Figs. 3 and 4). On the LMA side, the resulting current density localization leads to short Sand's time and promotes dendrite initiation. This localized dendrite formation accelerates the consumption of active Li (**I**, **J**, **L**, **8**, **9**, **10**, **13** and **14** in Figs. 3 and 4) and deteriorates the surface irregularity of the anode.

Stack pressure is also recognized as an important cell parameter influencing battery lifespan, as the unique creep and plastic deformation properties of metallic Li make its deposit morphology highly sensitive to external mechanical constraints. According to Newman's elasticity theory, LMA deformations occur when the applied stress exceeds its yield strength, with viscoelastic behaviour directly driving plastic deformation[112]. The yield strength of polycrystalline Li is dependent on dendrite size, for example, 105 MPa for a dendrite diameter of 1.39 μm but drops below 20 MPa for 9.45 μm (ref. 113). Thus, appropriate stack pressure modulates the mechanical behaviour of Li deposits, enabling viscoelastic deformation that facilitates planar and dendrite-free Li growth. Similarly, theoretical and experimental findings reveal that separators with a high shear modulus (>7 GPa, ~1.8 times that of metallic Li) can also suppress dendrite formation[114]. The concept of driving Li deposits towards planar morphology via mechanical deformation has prompted the development of separator coatings that integrate high ionic conductivity with robust mechanical strength[115]. Although stack pressure can suppress dendrite growth[116], improve CE_{Li}[39], densify dead Li layer, and reduce cell swelling[117], the viscoelastic nature of metallic Li causes time-dependent creep under constant stress[118]. The creep behaviour of metallic Li along both the longitudinal and transverse directions induces strain in the separator and cathode electrode, which also intensifies electric-field-edge effects in mechanically unconstrained overhang regions[119]. In addition to applying appropriate stack pressure that accounts for inelastic deformations of Li, replacing pure Li with Li alloys as anodes can alleviate creep deformation[120], with the trade-off of lower theoretical capacity.

Influenced by high-areal-capacity Li plating, size dimensions and stack pressure, LMBs are subjected to increasingly complex and self-reinforcing multi-physics degradation involving electrochemical, chemical, thermal, mechanical and fluid dynamics[111] (Box 1). First, a non-uniform current density distribution magnifies local disparities during high-areal-capacity Li plating, which induce electrolyte consumption, dead Li formation and thickness inhomogeneity of a cell (**K**, **M**, **N**, **8** and **9** in Figs. 3 and 4). Second, in-plane variations in cell flatness concentrate pressure in thicker regions, forming hotspots that locally accelerate electrochemical kinetics through mechanical-electrochemical coupling effects. Third, given that LLOs can accommodate Li beyond their stoichiometric limits during discharging[36], regions with elevated kinetics tends to intercalate more Li^+ back into cathode. Once surplus Li occupies the TM-O lattice and Li layer, it introduces

Box 1 | Interdependent degradation mechanisms of LMBs

Lifespan failure of LMBs is driven by complex and interdependent interactions among key battery materials, cell parameters and electrochemical processes, as illustrated in the figure. On the left side of the figure, critical cell parameters, such as high working voltage, low electrolyte-to-capacity (*E*/*C*) ratio, high areal cathode loading, electrode size and low anode-capacity to cathode-capacity (*N*/*P*) ratio, are necessary to achieve specific energies exceeding 600 Wh kg^{-1}, but they also act as driving factors for failure. On the right side of the figure, the associated macroscopic manifestations, such as gas evolution, cell-level resistance, cathode failure, concentration polarization, exhaustion of lithium metal anode (LMA), and cell swelling, represent the detectable outcomes of internal degradation pathways.

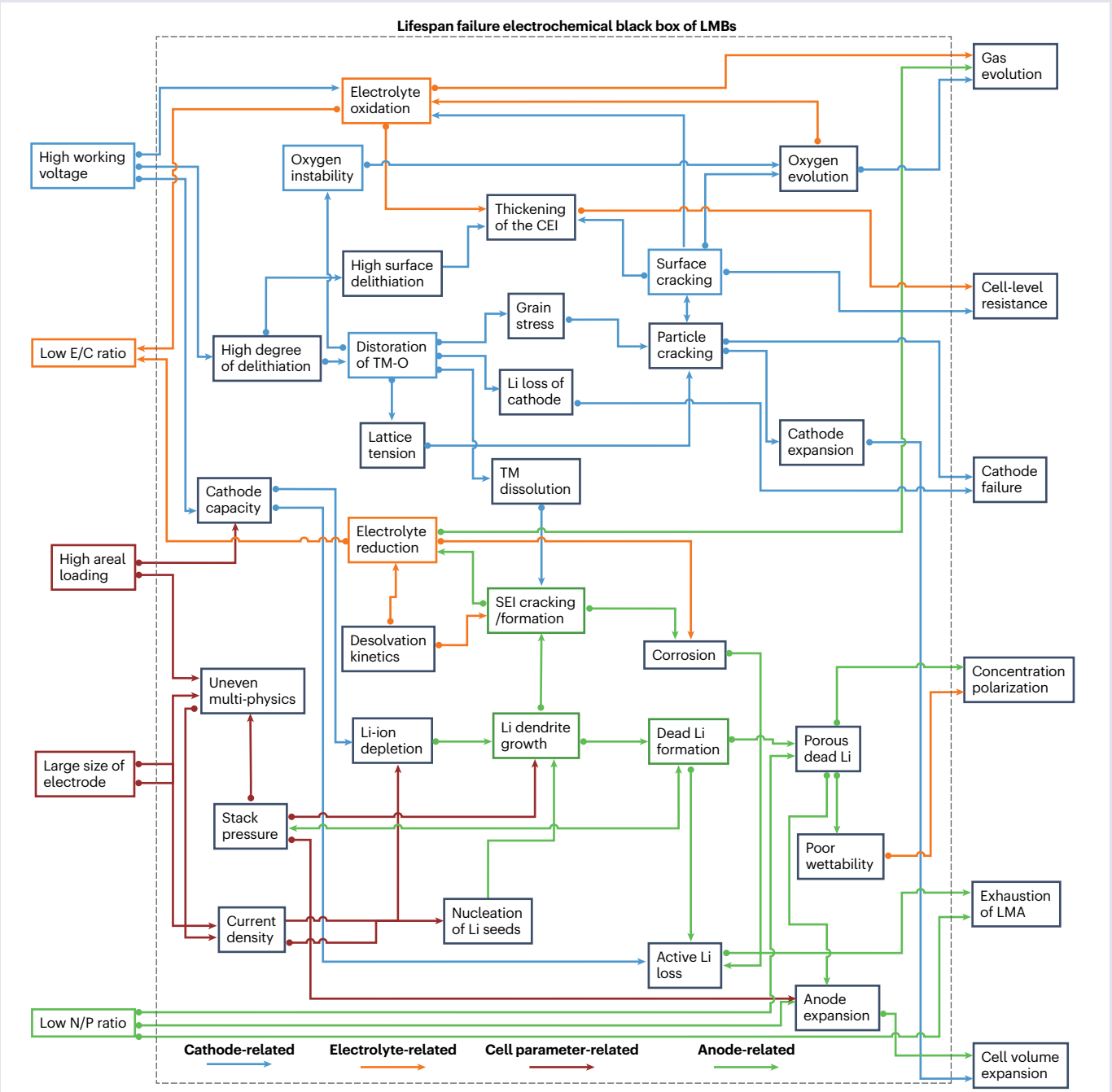

(continued from previous page)
The dashed box represents the 'electrochemical black box' of LMBs, wherein important but hidden failure origins are located. These are believed to mainly arise from oxygen-redox reaction (blue arrows), Li plating–stripping (green arrows), electrolyte decomposition (orange arrows), and cell-level design factors (dark red arrows). Although certain failure features can be characterized through electrochemical methods, many remain difficult to identify owing to the coupled nature of these processes. Specifically, the upper section of the figure highlights oxygen-redox-related failures and transition metal (TM) framework instability, which are mainly caused by the cathode and electrolyte, with additional influence from design parameters. The lower section of the figure illustrates anode-related failures, which result from the combined effects of the cathode, anode, electrolyte and overall cell design. These interconnected mechanisms increase the sensitivity of LMB lifespans to minor variations in cell design and key materials. Therefore, understanding LMB failure requires a holistic, cell-level perspective, one that considers not only the degradation of individual material but also the complex failure modes that emerge from their interdependent interactions. CEI, cathode–electrolyte interphase; SEI, solid electrolyte interphase; TM-O, transition metal–oxygen.

cathode degradation. Fourth, such hotspots also enhance delithiation kinetics in corresponding cathode regions, which aggravate TM-O lattice distortions and increase localized Li plating capacity. Consistent with this, concentrated stack pressure propagates across the cell, triggering cathode particle pulverization. Additionally, Joule heat accumulation and unstable surface structures further amplify surface degradation and oxygen release of the cathode. Fifth, reactive oxygen and heat promote sustained electrolyte decomposition to increase interfacial resistance (**C**, **L**, **6** and **12** in Figs. 3 and 4), which hinder Li intercalation into the cathode, resulting in a reduced $CE_{cathode}$ and capacity fading. Rising cell impedance (**A**, **C**, **L**, **M**, **N**, **6**, **7**, **8** and **12** in Figs. 3 and 4) also prolongs the time under constant-voltage charging, exposing cells to high-voltage stress, compromising cathode–electrolyte interfacial stability. Last, this cascading interplay, driven by extreme cell parameters, forms a vicious feedback loop between the cathode and anode, seriously affecting the lifespan of LMBs.

Cell assembly-induced failure chemistry

Cell engineering throughout the assembly process including slurry preparation, electrode drying, cell stacking and packaging, and chemical formation serves as key factors in determining lifespan. Strict dew point control during the entire assembly is essential. High ambient moisture enables residual bases (such as LiOH and Li_2CO_3) on LLOs to initiate nucleophilic reactions of polyvinylidene fluoride and the gelation of a cathode slurry[121], increasing slurry viscosity and impairing the homogeneity of thick electrodes. Electrode-level engineering, particularly optimized drying protocols, is important to balance areal loading and compacted density with appropriate electronic conductivity, ionic diffusivity and porosity in porous and thick cathodes[122]. For instance, narrowing the cathode particle size distribution improves conductivity and ion transportation but increases surface reactivity[123]. At the same time, incorporated multi-dimensional conductive networks (such as carbon nanotubes, graphene and acetylene black) enhance charge transfer yet risks slurry agglomeration and severe electrolyte decomposition[124]. During stacking, thin Li foils are prone to wrinkling and bending, compromising cell flatness and creating localized hotspots. Although attaching Cu foils as current collectors helps to prevent bending and facilitate stacking, concerns regarding reduced specific energy and galvanic corrosion remain[97]. Precise alignment of thin and large-sized Li foils with cathodes and separators is also important to eliminate electric fields at overhang edges and improve thermal safety[119]. Meanwhile, the highly reactive LMA readily reacts with moisture, CO_2, N_2, O_2 and trace particulates present in the ambient environment[9], which not only degrade their creep behaviour[125] but also accelerate self-discharge rates and promote localized micro-short circuits by serving as nucleation sites for Li dendrite growth. Unlike LIBs, packaging in LMBs must accommodate the repetitive volume fluctuations of cells during Li plating–stripping, posing considerable challenges for practical applications. Innovative cell packaging designs, such as QuantumScape's FlexFrame with hybrid pouch-prismatic architecture using a rigid frame to support the stack edges and flexible polymer laminates to accommodate expansion, may offer viable solutions. As the final step before sealing, initial chemical formation not only activates lattice oxygen capacity of LLOs[126] and establishes robust interphase on both electrodes[127,128] but also removes residual moisture and trapped gases, exerting a profound influence on long-term stability[129].

Chemical failure under operating conditions

Common battery operating conditions, including fast charge–discharge protocols and calendar ageing under high temperature, humidity and state-of-charge, affect the stability of LMBs. The fast-charging capability is closely related to cathode characteristics, such as delithiation resistance and cathode morphology (such as polycrystalline structures, particle size distribution and particle morphology). Rapid delithiation induces considerable lattice strain and distortion, propagating intragranular and intergranular cracks[130]. In addition, charging protocols directly affect the formation, density, size and crystallography of Li nuclei. The mismatch between rapid electroplating kinetics and limited ion diffusion promotes interfacial ion depletion. This depletion, in turn, leads to electrolyte reduction, the formation of uneven interphases, and charge inhomogeneity, which collectively initiate Li dendrite growth. Although some studies suggest that localized thermal effects from high current density may soften metallic Li in favour for flat morphology[131], applying such mechanisms at practical charge rates above 10*C* (wherein the applied current is ten times the nominal capacity) remains challenging. Pulse-charge protocols have emerged to modulate interfacial Li^+ concentration gradients by providing relaxation intervals, helping to recover interface homogeneity[132]. As discussed above, dead Li primarily forms during stripping processes, which means that the discharge current density governs both stripping modes and the integrity of Li removal[133]. Notably, many studies report higher discharge rates than their corresponding charge rates, for example, the charge–discharge rates of 0.1*C*/0.2*C* (ref. 35), 0.1*C*/0.3*C* (ref. 107), 0.2*C*/0.3*C* (ref. 133) or 0.2*C*/0.5*C* (ref. 22). Whether slower discharge rates, similar to slower electroplating, consistently yield improved CE_{Li} remains an open question. For polycrystalline LLOs, high discharge rates not only limit capacity utilization and lower voltage plateaux but also hinder Li^+ intercalation, promoting the Li/TM mixing. During high-temperature calendar ageing at 100% state-of-charge, interfacial stability is severely challenged. Accelerated dissolution and regeneration of interphases under both reductive and oxidative environments[134] enhance electron tunnelling

across the electrolyte–electrode interface, especially at highly delithiated near-surface regions of a cathode. High delithiation degrees under high temperatures trigger bulk oxygen release along grain boundaries and severe anisotropic lattice contraction in cathodes. Meanwhile, SEI instability under these conditions also induces continuous chemical and galvanic corrosion[135], which contributes to high self-discharge rates[136] and cumulative active Li loss[137]. As a result, the impedance increases after calendar ageing leads to a sharp drop in capacity, impairing battery function and limiting the lifespan.

Summary and future perspectives

The dual-Li-reservoir nature of LMBs presents unique challenges in identifying battery failure stages, making the tracking of active Li loss between electrodes an important task in failure analysis. Beyond intrinsic material degradation from oxygen-redox reactions and electrochemical Li plating–stripping, this Review thoroughly examines the critical effects of extrinsic factors on LMB lifespan, such as aggressive cell parameters, assembly processes and harsh operating conditions. We further outline the complex degradation pathways and map the 'electrochemical black box' of LMBs. The self-reinforcing degradation loops and the invisible Li consumption within LMA obscure accurate failure identification using conventional methods. At present, deciphering the lifespan conundrum, thus, demands advanced diagnostic tools to bridge current knowledge gaps across multiple time and spatial scales.

During oxygen-redox reactions in LLOs[138–141], excess energy introduced during initial electrochemical processes is stored in the lattice, inducing irreversible structural disorder with the distortion of the oxygen framework. This drives the lattice into a nonequilibrium state[142]. As higher specific energy targets demand greater oxygen-redox capacity contributions, the degree of lattice disorder increases, elevating the irreversibility of oxygen-redox-related capacity and cathode degradation. Thus, quantifying the relationship between oxygen-redox reversibility and LLO degradation is critical for rational cathode design. Studies have proposed evaluating structural disorder in LLOs as a promising approach[143]. Temperature-induced or pressure-induced structural relaxation can drive a disordered lattice back towards equilibrium, reflected by abnormal negative thermal expansion or a negative Poisson ratio[144]. By thermally driving the reordering of LLOs and characterizing the associated lattice parameter contraction, the degree of structural disorder can be quantitatively evaluated, offering new insights into the relationship between oxygen-redox capacity contributions and cathode degradation[4,142] (Fig. 5a). However, deeper insights require a broader structural physics perspective. At the particle level, understanding and visualizing the surface, subsurface, and bulk structural degradation of cathode particles provides critical evidence for elucidating the failure mechanisms and degradation pathways under practical operating conditions (Fig. 5b). Advanced TEM techniques, such as differential phase contrast-scanning TEM, integrated differential phase contrast-scanning TEM[4], and electron ptychography, enable atomic-level visualization of lattice disorder and TM-O distortion. Various operando characterization techniques, including X-ray and neutron diffractions, extended X-ray absorption fine structure, and solid-state nuclear magnetic resonance have been extensively applied to investigate the LLOs[145]. Moving forward, multi-scale, in situ and operando diagnostic techniques are essential to correlate valence states, atomic-level disorder and particle morphology, and to map the temporal sequence of surface degradation, crack propagation and lattice collapse.

The key challenges in understanding the degradation of Li plating–stripping lies in operando visualization of Li nucleation, growth, stripping and mechanical deformation under practical Ah-level cell configurations[146] (Fig. 5c). Post-mortem studies often miss dendritic Li morphology owing to mechanical constraints during operation. Future work should develop high-resolution, operando imaging for practical cells that can capture mechanical-electrochemical interactions such as void formation, Li creep, plastic deformation and non-uniform plating across electrode under stack pressure[147]. Real-time observation across multiple spatial and temporal scales, such as optical, X-ray and electron microscopy, will be indispensable for uncovering the dynamic behaviour.

For LLOs operating at 4.8 V, electrolyte stability becomes a decisive factor for long-life LMBs. Conventional electrochemical techniques, such as linear sweep voltammetry and chronoamperometry, typically conducted on inert electrodes and influenced by cell resistance[148], fail to decouple chemical and electrochemical oxidation of electrolytes[8]. However, chemical oxidation at highly delithiated cathode surfaces, particularly with reactive TM sites or reactive oxygen species (Fig. 5d), contributes substantially to electrolyte decomposition. Future efforts should treat electrolyte chemical oxidation as a quantifiable chemical reaction, evaluating its thermodynamic and kinetic characteristics to guide rational electrolyte design[98,149]. In fact, the reduction and oxidation of an electrolyte are closely tied to the solvation structure evolution at electrolyte–electrolyte interfaces within the electrical double layer (EDL). Inside the Helmholtz plane, partially desolvated solvation structures dominate the interphase composition and chemical stability of an electrolyte. Probing desolvation dynamics at the EDL, including reorganization of solvent–Li^+–anion clusters, anion adsorption and the desolvation sequence (Fig. 5e), enables researchers to clarify their correlation with interphase components, but this still remains challenging owing to the unique nanoscale structure of the EDL differing completely from those of bulk electrolytes. Surface-sensitive and time-resolved methods, such as surface-enhanced Raman spectroscopy[150], attenuated total reflectance Fourier transform infrared spectroscopy (FTIR)[151], femtosecond FTIR[152] and sum frequency generation spectroscopy[153], offer the potential to resolve these dynamics. When integrated with ab initio molecular dynamics simulations and machine learning (such as electrolyte molecular universe), they present great promise for expediting new electrolyte formulations[154]. Furthermore, the electrolyte has critical roles in precisely regulating the formation of desired interphases under both oxidative and reductive environments. These interphases undergo dynamic changes in composition and thickness during cycling and calendar ageing. However, most existing studies rely heavily on localized, often qualitative, observations[155]. To establish predictive composition–function relationships, global quantitative composition analysis is needed. Innovative methods, such as titration gas chromatography[156], which can be combined with titration mass spectrometry[157] and Karl Fischer titration[158], offer pathways to determine the overall interphase composition (Fig. 5f). These methodologies can help correlate component evolution, especially the inorganic-to-organic ratio, to understand how interphase chemistry contributes to cell degradation under operational conditions.

The dilemma in developing electrolytes for 600 Wh kg^{-1} LMBs is the need to simultaneously achieve high CE_{Li} and an extreme oxidative tolerance. Electrolytes designed for high-voltage NCM cathodes often decompose on the LLO owing to the harsher oxidation environment of oxygen-redox reactions, causing severe impedance growth and limited capacity. Typically, oxidation-tolerant solvents such as

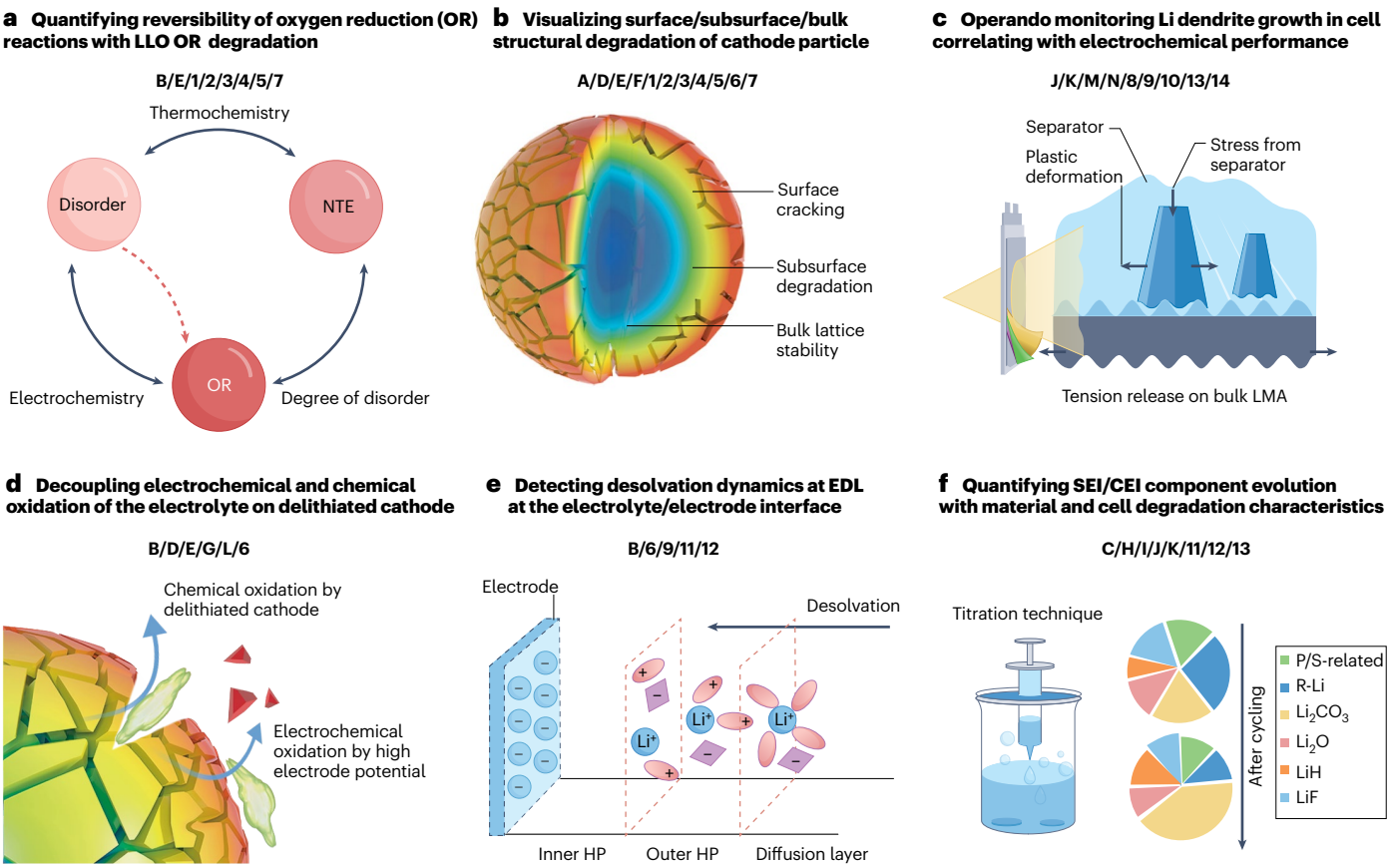

Fig. 5 | Knowledge gaps and advanced characterization techniques required to elucidate the detailed failure pathways of lithium metal batteries with specific energies beyond 600 Wh kg^{-1}. The labels 1–14 and A–N respectively correspond to the related material-level and cell-level degradation concerns discussed in Fig. 3. Techniques for quantifying the reversibility of oxygen-redox reaction with Li-rich layered oxide (LLOs) degradation and the impact of negative thermal expansion (NTE) (part **a**), and visualizing the surface, subsurface and bulk structural degradation of cathode particles (part **b**). **c**, Advanced operando characterization techniques are crucial for monitoring mechanical properties and the behaviour of lithium metal anode (LMA) under stack pressure in practical cell-level conditions, and the techniques also correlate the relationship of LMA behaviour with Coulombic efficiencies for Li plating–stripping. **d**, The establishment of novel methodologies is required to decouple the thermodynamic and kinetic differences between chemical and electrochemical oxidation degradation of the electrolyte, enabling the assessment of anti-oxidation abilities of the electrolyte. **e**, Detecting desolvation dynamics within the inner and outer Helmholtz plane (HP) at charged electrode interfaces and electrical double layers (EDLs). **f**, Quantitative titration techniques coupled with component analysis techniques are vital for elucidating the relationship between interphase component changes (of solid electrolyte interphases (SEIs) and/or cathode–electrolyte interphases (CEIs)) and battery degradation.

carbonates, sulfones and nitriles exhibit poor compatibility with Li (ref. 159), whereas ether-based solvents, which offer high CE_{Li}, lack the necessary oxidative stability. Strategies such as fluorination and localized high-concentration electrolytes have extended the stability of ethers up to 4.6 V for NCM cathodes, but this is still insufficient for the oxygen-redox reaction of LLOs. The underlying issue is that diluents with weak coordination abilities in localized high-concentration electrolytes are often excluded from the inner solvation sheath at the cathode interface, leaving the vulnerable ether-based solvents exposed to decomposition. Similarly, advanced formulations struggle to achieve a CE_{Li} above 99.90% under practical high-areal-capacity Li plating–stripping conditions. This highlights the urgent need for novel solvents that combine strong salt dissociation, high oxidative stability and favourable SEI-forming properties[160]. In parallel, sacrificial additives that promote interphase formation are being explored to mitigate oxidative stress and regulate SEI chemistry[161]. However, for cathode-stabilizing additives such as nitriles and sulfones, their concentration must be carefully limited to avoid an unacceptable rise in cell impedance. When evaluating additives for LMAs, the testing protocols are critical. The assessments should be performed in high-areal-capacity Li/Cu coin cells or practical LMB cells, as Li symmetric coin cells often yield misleading results owing to soft-shorting. Finally, novel lithium salts with asymmetric structures that balance dissociation and stability represent another promising frontier, underscoring the need for greater investment in organic synthesis to realize these new materials with high purity and yield[162].

Beyond lifespan, thermal safety throughout the entire lifecycle must also be considered. Unlike LIBs, wherein a 20% capacity fade reflects Li loss from the cathode or Li trapped in the anode, a similar capacity fade in LMBs indicates the additional transformation of the LMA into a

layer of micro-scale dead Li. Owing to its high surface area and chemical reactivity with organic solvents[163,164], LMBs exhibit more severe thermal failure features[165]. Although the thick SEI on LMAs may suppress initial exothermic reactions and impedance growth during cycling can lower the short-circuit current, these effects may misleadingly suggest that the thermal failure onset temperature (T_1) of aged LMBs is not particularly high[166]. However, ongoing heat release and thick SEI decomposition progress can lead to the separator melting and large-area short circuits in the cell, triggering considerable Joule heating. This triggers the rapid temperature rise that melts metallic Li, which then makes direct contact between the cathode and melted Li, initiating an even more extensive internal short circuit. As the temperature spikes, the high-surface-area, polycrystalline structure of LLOs exacerbate these side reactions. Where the cathode cracks, exposed and high-valence TMs are reduced as the electrolyte oxidizes, releasing heat, gases and radicals. Concurrently, oxygen bonds weaken, releasing reactive oxygen and flammable gases, whereas oxygen vacancies induce structural collapse, leading to rapid particle pulverization. Finally, self-accelerating decomposition pushes the cell to a second thermal runaway stage (T_2). Under these conditions, the maximum temperature during thermal runaway can exceed 1,000 °C in cycled LMBs[167], posing considerable thermal risks, particularly in large-capacity (>100 Ah) cells. Improving LMB thermal safety in the future requires particular attention in two areas. First, minimizing early-stage heat generation requires the optimization of separator melting and shutdown temperatures[168], balancing impedance between electrodes and current collectors, and developing smart electrolytes[169]. Second, the rate of temperature rise before T_2 can be lowered by improving heat dissipation of a cell and pack, optimizing interphase chemistry of electrodes, using flame-retardant electrolytes[170], and using Li alloys to prevent melting.

Addressing the above scientific challenges associated with LMB failures provides valuable insights into material optimization, battery designs, cell manufacturing and performance evaluations. With continued efforts and collaborations between academia and industry, substantial progress can be achieved to enable the operation of safe and durable LMBs capable of reaching specific energies beyond 600 Wh kg^{-1}.

Published online: 20 February 2026

References

1. Li, Q., Yu, X., Li, H. & Chen, L. The road towards high-energy-density batteries. *Innov. Energy* **1**, 100005 (2024).
2. Choi, J. W. & Aurbach, D. Promise and reality of post-lithium-ion batteries with high energy densities. *Nat. Rev. Mater.* **1**, 1–16 (2016).
3. Shi, Z. et al. Self-regulatory lean-electrolyte flow for building 600 Wh kg^{-1}-level rechargeable lithium batteries. *Adv. Mater.* **37**, 2419377 (2025).
4. Qiu, B. et al. Negative thermal expansion and oxygen-redox electrochemistry. *Nature* **640**, 941–946 (2025).
5. Fang, C., Wang, X. & Meng, Y. S. Key issues hindering a practical lithium-metal anode. *Trends Chem.* **1**, 152–158 (2019).
6. Zhang, M. et al. Pushing the limit of 3*d* transition metal-based layered oxides that use both cation and anion redox for energy storage. *Nat. Rev. Mater.* **7**, 522–540 (2022).
7. Qiu, B., Qiao, Y., Li, B. & Liu, Z. Next-generation cathode materials for ultrahigh-energy batteries. *Next Mater.* **1**, 100034 (2023).
8. Rinkel, B. L., Hall, D. S., Temprano, I. & Grey, C. P. Electrolyte oxidation pathways in lithium-ion batteries. *J. Am. Chem. Soc.* **142**, 15058–15074 (2020).
9. He, X. et al. The passivity of lithium electrodes in liquid electrolytes for secondary batteries. *Nat. Rev. Mater.* **6**, 1036–1052 (2021).
10. Hobold, G. M. et al. Moving beyond 99.9% coulombic efficiency for lithium anodes in liquid electrolytes. *Nat. Energy* **6**, 951–960 (2021).
11. Yang, Y. et al. High-efficiency lithium-metal anode enabled by liquefied gas electrolytes. *Joule* **3**, 1986–2000 (2019).
This work reports an average CE_{Li} of 99.9%.
12. Yang, W., Chen, A., He, P. & Zhou, H. Advancing lithium metal electrode beyond 99.9% coulombic efficiency via super-saturated electrolyte with compressed solvation structure. *Nat. Commun.* **16**, 1–12 (2025).
13. Liu, J. et al. Pathways for practical high-energy long-cycling lithium metal batteries. *Nat. Energy* **4**, 180–186 (2019).
This perspective highlights the need to integrate key material and cell design principles in LMB research and evaluation.
14. Hatzell, K. et al. Aligning lithium metal battery research and development across academia and industry. *Joule* **8**, 1550–1555 (2024).
This commentary highlights the need to align LMB academic research with practical industrial development.
15. Zhang, K. et al. A high-performance lithium metal battery with ion-selective nanofluidic transport in a conjugated microporous polymer protective layer. *Adv. Mater.* **33**, 2006323 (2021).
16. Zhao, P. et al. Constructing self-adapting electrostatic interface on lithium metal anode for stable 400 Wh kg^{-1} pouch cells. *Adv. Energy Mater.* **12**, 2200568 (2022).
17. Wang, Z. et al. High-performance localized high-concentration electrolytes by diluent design for long-cycling lithium metal batteries. *Chin. Chem. Lett.* **35**, 108570 (2024).
18. Zhang, Q. K. et al. Reforming the uniformity of solid electrolyte interphase by nanoscale structure regulation for stable lithium metal batteries. *Angew. Chem. Int. Ed.* **135**, e202306889 (2023).
19. Wang, Z. et al. Highly soluble organic nitrate additives for practical lithium metal batteries. *Carbon Energy* **5**, e283 (2023).
20. Zhang, Y. et al. Enabling 420 Wh kg^{-1} stable lithium-metal pouch cells by lanthanum doping. *Adv. Mater.* **35**, 2211032 (2023).
21. Zhang, Q.-K. et al. Homogeneous and mechanically stable solid–electrolyte interphase enabled by trioxane-modulated electrolytes for lithium metal batteries. *Nat. Energy* **8**, 725–735 (2023).
22. Zhang, S. et al. Oscillatory solvation chemistry for a 500 Wh kg^{-1} Li-metal pouch cell. *Nat. Energy* **9**, 1285–1296 (2024).
23. Guo, J. C. et al. A self-reconfigured, dual-layered artificial interphase toward high-current-density quasi-solid-state lithium metal batteries. *Adv. Mater.* **35**, 2300350 (2023).
24. Ma, Q. et al. Formulating the electrolyte towards high-energy and safe rechargeable lithium–metal batteries. *Angew. Chem. Int. Ed.* **60**, 16554–16560 (2021).
25. Deng, W. et al. Competitive solvation-induced concurrent protection on the anode and cathode toward a 400 Wh kg^{-1} lithium metal battery. *ACS Energy Lett.* **6**, 115–123 (2020).
26. Qiao, R. et al. Non-fluorinated electrolytes with micelle-like solvation for ultra-high energy density lithium metal batteries. *Chem* **11**, 102306 (2024).
27. Tang, T. et al. Long-lifespan 522 Wh kg^{-1} lithium metal pouch cell enabled by compound additives engineering. *Angew. Chem. Int. Ed.* **64**, e202417471 (2025).
28. Jie, Y. et al. Towards long-life 500 Wh kg^{-1} lithium metal pouch cells via compact ion-pair aggregate electrolytes. *Nat. Energy* **9**, 987–998 (2024).
29. Su, H. et al. Achieving practical high-energy-density lithium-metal batteries by a dual-anion regulated electrolyte. *Adv. Mater.* **35**, 2301171 (2023).
30. Ji, H. et al. Liquid–liquid interfacial tension stabilized Li-metal batteries. *Nature* **643**, 1255–1262 (2025).
31. Wei, Z. et al. Eliminating oxygen releasing of Li-rich layered cathodes by tuning the distribution of superlattice domain. *Mater. Today Energy* **27**, 101039 (2022).
32. Luo, P. et al. Understanding and mitigating acidic species in all-fluorinated electrolytes for a stable 572 Wh kg^{-1} lithium metal battery (LMB). *Energy Storage Mater.* **78**, 104234 (2025).
33. Liu, X. et al. 570 Wh kg^{-1}-grade lithium metal pouch cell with 4.9 V highly Li^+ conductive armor-like cathode electrolyte interphase via partially fluorinated electrolyte engineering. *Adv. Mater.* **36**, 2401505 (2024).
34. Huang, H. et al. Delocalized electrolyte design enables 600 Wh kg^{-1} lithium metal pouch cells. *Nature* **644**, 660–667 (2025).
35. He, Y. et al. Optimizing Li plating behavior via controlling areal capacity of a cathode for cycling stability on 600 Wh kg^{-1} lithium-metal batteries. *ACS Appl. Mater. Interfaces* **16**, 33475–33484 (2024).
36. Li, Q., Yang, Y., Yu, X. & Li, H. A 700 W·h·kg^{-1} rechargeable pouch type lithium battery. *Chin. Phys. Lett.* **40**, 048201 (2023).
This work reports the 700 Wh kg^{-1} LMB prototype by using LMA and LLOs.
37. He, M. et al. Industry needs for practical lithium-metal battery designs in electric vehicles. *Nat. Energy* **9**, 1199–1205 (2024).
38. Menkin, S. et al. Insights into soft short circuit-based degradation of lithium metal batteries. *Faraday Discuss.* **248**, 277–297 (2024).
39. Deng, W. et al. Quantification of reversible and irreversible lithium in practical lithium-metal batteries. *Nat. Energy* **7**, 1031–1041 (2022).
This work reports the method for quantifying CE_{Li} in Ah-level LMBs.
40. Wood, K. N. et al. Dendrites and pits: untangling the complex behavior of lithium metal anodes through operando video microscopy. *ACS Cent. Sci.* **2**, 790–801 (2016).
41. Chen, K. H. et al. Dead lithium: mass transport effects on voltage, capacity, and failure of lithium metal anodes. *J. Mater. Chem. A* **5**, 11671–11681 (2017).
This work highlights the presence and impact of the dead Li layer on the degradation pathways of LMBs.
42. Lu, D. et al. Failure mechanism for fast-charged lithium metal batteries with liquid electrolytes. *Adv. Energy Mater.* **5**, 1400993 (2015).
43. Xiang, Y. X. et al. Quantitatively analyzing the failure processes of rechargeable Li metal batteries. *Sci. Adv.* **7**, eabj3423 (2021).

44. Zeng, L. et al. Voltage decay of Li-rich layered oxides: mechanism, modification strategies, and perspectives. *Adv. Funct. Mater.* **33**, 2213260 (2023).
45. House, R. A. et al. First-cycle voltage hysteresis in Li-rich 3*d* cathodes associated with molecular O_2 trapped in the bulk. *Nat. Energy* **5**, 777–785 (2020).
46. Xu, B., Fell, C. R., Chi, M. & Meng, Y. S. Identifying surface structural changes in layered Li-excess nickel manganese oxides in high voltage lithium ion batteries: a joint experimental and theoretical study. *Energy Environ. Sci.* **4**, 2223–2233 (2011).
47. Yan, P. et al. Injection of oxygen vacancies in the bulk lattice of layered cathodes. *Nat. Nanotechnol.* **14**, 602–608 (2019).
48. Li, X. et al. Dependence of initial capacity irreversibility on oxygen framework chemistry in Li-rich layered cathode oxides. *Energy Environ. Mater.* **7**, e12722 (2024).
49. Liu, T. et al. Origin of structural degradation in Li-rich layered oxide cathode. *Nature* **606**, 305–312 (2022).
This work highlights the role of lattice strain or displacement in driving voltage decay and oxygen loss in LLOs.
50. Croy, J. R., Balasubramanian, M., Gallagher, K. G. & Burrell, A. K. Review of the US Department of Energy's "deep dive" effort to understand voltage fade in Li- and Mn-rich cathodes. *Acc. Chem. Res.* **48**, 2813–2821 (2015).
51. Eum, D. et al. Voltage decay and redox asymmetry mitigation by reversible cation migration in lithium-rich layered oxide electrodes. *Nat. Mater.* **19**, 419–427 (2020).
52. Wang, E. et al. Al/Ti synergistic doping enhanced cycle stability of Li-rich layered oxides. *Adv. Funct. Mater.* **32**, 2201744 (2022).
53. Qing, R. P. et al. Enhancing the kinetics of Li-rich cathode materials through the pinning effects of gradient surface Na^+ doping. *Adv. Energy Mater.* **6**, 1501914 (2016).
54. Li, Q. et al. K^+-doped $Li_{1.2}Mn_{0.54}Co_{0.13}Ni_{0.13}O_2$: a novel cathode material with an enhanced cycling stability for lithium-ion batteries. *ACS Appl. Mater. Interfaces* **6**, 10330–10341 (2014).
55. Wang, M., Chen, L., Liu, M., Chen, Y. & Gu, Y. Enhanced electrochemical performance of La-doped Li-rich layered cathode material. *J. Alloys Compd.* **848**, 156620 (2020).
56. Gao, Y., Wang, X., Ma, J., Wang, Z. & Chen, L. Selecting substituent elements for Li-rich Mn-based cathode materials by density functional theory (DFT) calculations. *Chem. Mater.* **27**, 3456–3461 (2015).
57. Wang, M. et al. Enhanced electrochemical performances of cerium-doped Li-Rich $Li_{1.2}Ni_{0.13}Co_{0.13}Mn_{0.54}O_2$ cathode materials. *J. Alloys Compd.* **861**, 158000 (2021).
58. Peng, Z. et al. Enhanced electrochemical performance of layered Li-rich cathode materials for lithium ion batteries via aluminum and boron dual-doping. *Ceram. Int.* **45**, 4184–4192 (2019).
59. Seaby, T., Lin, T.-E., Hu, Y.-X., Yuan, Q.-H. & Wang, L.-Z. An analysis of F-doping in Li-rich cathodes. *Rare Met.* **41**, 1771–1796 (2022).
60. Yan, H., Li, B., Yu, Z., Chu, W. & Xia, D. First-principles study: tuning the redox behavior of lithium-rich layered oxides by chlorine doping. *J. Phys. Chem. C* **121**, 7155–7163 (2017).
61. Nayak, P. K. et al. Al doping for mitigating the capacity fading and voltage decay of layered Li and Mn-rich cathodes for Li-ion batteries. *Adv. Energy Mater.* **6**, 1502398 (2016).
62. Dahiya, P., Ghanty, C., Sahoo, K., Basu, S. & Majumder, S. Suppression of voltage decay and improvement in electrochemical performance by zirconium doping in Li-rich cathode materials for Li-ion batteries. *J. Electrochem. Soc.* **165**, A3114 (2018).
63. Feng, Z. et al. Adjusting oxygen redox reaction and structural stability of Li- and Mn-rich cathodes by Zr-Ti dual-doping. *ACS Appl. Mater. Interfaces* **14**, 5308–5317 (2022).
64. Yang, P. et al. A gradient doping strategy toward superior electrochemical performance for Li-rich Mn-based cathode materials. *Small* **19**, 2207797 (2023).
65. Lu, C. et al. Enhanced electrochemical performance of Li-rich $Li_{1.2}Mn_{0.52}Co_{0.08}Ni_{0.2}O_2$ cathode materials for Li-ion batteries by vanadium doping. *Electrochim. Acta* **209**, 448–455 (2016).
66. Meng, J. et al. Modulating crystal and interfacial properties by W-gradient doping for highly stable and long life Li-rich layered cathodes. *Adv. Funct. Mater.* **32**, 2113013 (2022).
67. Yang, J. et al. Encouraging voltage stability upon long cycling of Li-rich Mn-based cathode materials by Ta–Mo dual doping. *ACS Appl. Mater. Interfaces* **13**, 25981–25992 (2021).
68. Eum, D. et al. Electrochemomechanical failure in layered oxide cathodes caused by rotational stacking faults. *Nat. Mater.* **23**, 1093–1099 (2024).
69. Zheng, J. & Archer, L. A. Crystallographically textured electrodes for rechargeable batteries: symmetry, fabrication, and characterization. *Chem. Rev.* **122**, 14440–14470 (2022).
70. Celeste, A. et al. On the elusive crystallography of lithium-rich layered oxides: novel structural models. *Small Methods* **8**, 2301466 (2024).
71. Yin, C. et al. Structural insights into composition design of Li-rich layered cathode materials for high-energy rechargeable battery. *Mater. Today* **51**, 15–26 (2021).
72. Zeng, L. et al. Quenching-induced lattice modifications endowing Li-rich layered cathodes with ultralow voltage decay and long life. *Energy Environ. Sci.* **18**, 284–299 (2025).
73. Csernica, P. M. et al. Persistent and partially mobile oxygen vacancies in Li-rich layered oxides. *Nat. Energy* **6**, 642–652 (2021).
74. Wandt, J., Freiberg, A. T., Ogrodnik, A. & Gasteiger, H. A. Singlet oxygen evolution from layered transition metal oxide cathode materials and its implications for lithium-ion batteries. *Mater. Today* **21**, 825–833 (2018).
75. Marie, J.-J. et al. Trapped O_2 and the origin of voltage fade in layered Li-rich cathodes. *Nat. Mater.* **23**, 818–825 (2024).
76. Lee, S., Su, L., Mesnier, A., Cui, Z. & Manthiram, A. Cracking vs. surface reactivity in high-nickel cathodes for lithium-ion batteries. *Joule* **7**, 2430–2444 (2023).
77. Zhu, Z. et al. Gradient Li-rich oxide cathode particles immunized against oxygen release by a molten salt treatment. *Nat. Energy* **4**, 1049–1058 (2019).
78. Qiu, B. et al. Gas–solid interfacial modification of oxygen activity in layered oxide cathodes for lithium-ion batteries. *Nat. Commun.* **7**, 12108 (2016).
This work reports a method for constructing surface oxygen vacancy on LLOs for practical application.
79. Li, A. et al. Enhancing cycling stability in Li-rich layered oxides by atomic layer deposition of $LiNbO_3$ nanolayers. *Solid State Ion* **417**, 116727 (2024).
80. Jung, R., Metzger, M., Maglia, F., Stinner, C. & Gasteiger, H. A. Chemical versus electrochemical electrolyte oxidation on NMC111, NMC622, NMC811, LNMO, and conductive carbon. *J. Phys. Chem. Lett.* **8**, 4820–4825 (2017).
81. Li, Y. et al. A novel 3D Li/Li_9Al_4/Li-Mg alloy anode for superior lithium metal batteries. *Adv. Funct. Mater.* **33**, 2213905 (2023).
82. Gao, P. et al. Optimization of magnesium-doped lithium metal anode for high performance lithium metal batteries through modeling and experiment. *Angew. Chem. Int. Ed.* **60**, 16506–16513 (2021).
83. Lu, Y. et al. The carrier transition from Li atoms to Li vacancies in solid-state lithium alloy anodes. *Sci. Adv.* **7**, eabi5520 (2021).
84. Wang, X. et al. Glassy Li metal anode for high-performance rechargeable Li batteries. *Nat. Mater.* **19**, 1339–1345 (2020).
85. Pei, A., Zheng, G., Shi, F., Li, Y. & Cui, Y. Nanoscale nucleation and growth of electrodeposited lithium metal. *Nano Lett.* **17**, 1132–1139 (2017).
86. Yan, K. et al. Selective deposition and stable encapsulation of lithium through heterogeneous seeded growth. *Nat. Energy* **1**, 1–8 (2016).
87. Deng, W., Zhou, X., Fang, Q. & Liu, Z. Microscale lithium metal stored inside cellular graphene scaffold toward advanced metallic lithium anodes. *Adv. Energy Mater.* **8**, 1703152 (2018).
88. Chazalviel, J.-N. Electrochemical aspects of the generation of ramified metallic electrodeposits. *Phys. Rev. A* **42**, 7355 (1990).
89. Bai, P., Li, J., Brushett, F. R. & Bazant, M. Z. Transition of lithium growth mechanisms in liquid electrolytes. *Energy Environ. Sci.* **9**, 3221–3229 (2016).
90. Wang, S. H. et al. Stable Li metal anodes via regulating lithium plating/stripping in vertically aligned microchannels. *Adv. Mater.* **29**, 1703729 (2017).
91. Alexander, G. V., Shi, C., O'Neill, J. & Wachsman, E. D. Extreme lithium-metal cycling enabled by a mixed ion- and electron-conducting garnet three-dimensional architecture. *Nat. Mater.* **22**, 1136–1143 (2023).
92. Hu, A. et al. An artificial hybrid interphase for an ultrahigh-rate and practical lithium metal anode. *Energy Environ. Sci.* **14**, 4115–4124 (2021).
93. Liu, Y. et al. Electro-chemo-mechanical modeling of artificial solid electrolyte interphase to enable uniform electrodeposition of lithium metal anodes. *Adv. Energy Mater.* **12**, 2103589 (2022).
94. Han, Z. et al. A protective layer for lithium metal anode: why and how. *Small Methods* **5**, 2001035 (2021).
95. Santhosha, A., Medenbach, L., Buchheim, J. R. & Adelhelm, P. The indium–lithium electrode in solid-state lithium-ion batteries: phase formation, redox potentials, and interface stability. *Batt. Supercaps* **4**, 1654–1654 (2021).
96. Sayavong, P. et al. Dissolution of the solid electrolyte interphase and its effects on lithium metal anode cyclability. *J. Am. Chem. Soc.* **145**, 12342–12350 (2023).
97. Lin, D. et al. Fast galvanic lithium corrosion involving a Kirkendall-type mechanism. *Nat. Chem.* **11**, 382–389 (2019).
98. Wang, H. et al. Application-driven design of non-aqueous electrolyte solutions through quantification of interfacial reactions in lithium metal batteries. *Nat. Nanotechnol.* **20**, 1034–1042 (2025).
99. Rynearson, L. et al. Speciation of transition metal dissolution in electrolyte from common cathode materials. *Angew. Chem. Int. Ed.* **136**, e202317109 (2024).
100. Sim, R., Su, L., Dolocan, A. & Manthiram, A. Delineating the impact of transition-metal crossover on solid-electrolyte interphase formation with ion mass spectrometry. *Adv. Mater.* **36**, 2311573 (2024).
101. Xu, H. et al. Impacts of dissolved Ni^{2+} on the solid electrolyte interphase on a graphite anode. *Angew. Chem. Int. Ed.* **134**, e202202894 (2022).
102. Jin, C. et al. Inhibiting and rejuvenating dead lithium in battery materials. *Nat. Rev. Chem.* **9**, 553–568 (2025).
103. Werres, M. et al. Origin of heterogeneous stripping of lithium in liquid electrolytes. *ACS Nano* **17**, 10218–10228 (2023).
104. Wang, C. et al. Tension-induced cavitation in Li-metal stripping. *Adv. Mater.* **35**, 2209091 (2023).
105. Sanchez, A. J. et al. Plan-view operando video microscopy of Li metal anodes: identifying the coupled relationships among nucleation, morphology, and reversibility. *ACS Energy Lett.* **5**, 994–1004 (2020).
106. Liu, H. et al. Plating/stripping behavior of actual lithium metal anode. *Adv. Energy Mater.* **9**, 1902254 (2019).
107. Niu, C. et al. Balancing interfacial reactions to achieve long cycle life in high-energy lithium metal batteries. *Nat. Energy* **6**, 723–732 (2021).
108. Liu, X. et al. Advances in multi-scale design and fabrication processes for thick electrodes in lithium-ion batteries. *Energy Rev.* **3**, 100066 (2024).
109. Kuang, Y., Chen, C., Kirsch, D. & Hu, L. Thick electrode batteries: principles, opportunities, and challenges. *Adv. Energy Mater.* **9**, 1901457 (2019).

110. Jiao, S. et al. Behavior of lithium metal anodes under various capacity utilization and high current density in lithium metal batteries. *Joule* **2**, 110–124 (2018).
111. Cai, X. et al. Characterization and quantification of multi-field coupling in lithium-ion batteries under mechanical constraints. *J. Energy Chem.* **95**, 364–379 (2024).
112. Monroe, C. & Newman, J. The impact of elastic deformation on deposition kinetics at lithium/polymer interfaces. *J. Electrochem. Soc.* **152**, A396 (2005).
113. Xu, C., Ahmad, Z., Aryanfar, A., Viswanathan, V. & Greer, J. R. Enhanced strength and temperature dependence of mechanical properties of Li at small scales and its implications for Li metal anodes. *Proc. Natl Acad. Sci. USA* **114**, 57–61 (2017).
114. Zhang, W. et al. Design principles of functional polymer separators for high-energy, metal-based batteries. *Small* **14**, 1703001 (2018).
115. Seo, J. et al. Recent progress of advanced functional separators in lithium metal batteries. *Small* **20**, 2312132 (2024).
116. Fang, C. C. et al. Pressure-tailored lithium deposition and dissolution in lithium metal batteries. *Nat. Energy* **6**, 987–994 (2021).
117. Liu, D. et al. Controlled large-area lithium deposition to reduce swelling of high-energy lithium metal pouch cells in liquid electrolytes. *Nat. Energy* **9**, 559–569 (2024).
118. Masias, A., Felten, N., Garcia-Mendez, R., Wolfenstine, J. & Sakamoto, J. Elastic, plastic, and creep mechanical properties of lithium metal. *J. Mater. Sci.* **54**, 2585–2600 (2019).
This work characterizes the elastic and plastic mechanical properties and creep behaviour of Li metal.
119. Huang, Y. et al. Mechanism of lithium plating and stripping in lithium-ion batteries induced by overhang failure defects. *Cell Rep. Phys. Sci.* **5**, 102299 (2024).
120. Krauskopf, T., Mogwitz, B., Rosenbach, C., Zeier, W. G. & Janek, J. Diffusion limitation of lithium metal and Li–Mg alloy anodes on LLZO type solid electrolytes as a function of temperature and pressure. *Adv. Energy Mater.* **9**, 1902568 (2019).
121. Lei, Y. et al. Surface modification of Li-rich Mn-based layered oxide cathodes: challenges, materials, methods, and characterization. *Adv. Energy Mater.* **10**, 2002506 (2020).
122. Wu, J. et al. From fundamental understanding to engineering design of high-performance thick electrodes for scalable energy-storage systems. *Adv. Mater.* **33**, 2101275 (2021).
123. Park, N.-Y. et al. Degradation mechanism of Ni-rich cathode materials: focusing on particle interior. *ACS Energy Lett.* **7**, 2362–2369 (2022).
124. Ji, W., Qu, H., Zhang, X., Zheng, D. & Qu, D. Electrode architecture design to promote charge-transport kinetics in high-loading and high-energy lithium-based batteries. *Small Methods* **5**, 2100518 (2021).
125. Dienemann, L. L., Saigal, A. & Zimmerman, M. A. Creep and anisotropy of free-standing lithium metal foils in an industrial dry room. *J. Electrochem. Energy* **18**, 040908 (2021).
126. Zhang, K. et al. Unveiling the influence of formation voltage on Li-rich layered oxide cathode. *Angew. Chem. Int. Ed.* **64**, e202515719 (2025).
127. Zhang, S. et al. The lasting impact of formation cycling on the Li-ion kinetics between SEI and the Li-metal anode and its correlation with efficiency. *Sci. Adv.* **10**, eadj8889 (2024).
128. Zhou, M. et al. Correlating the potential-holding formation protocol of solid–electrolyte interphases with improving calendar aging on lithium metal anode. *ACS Energy Lett.* **8**, 4702–4710 (2023).
129. Chang, W. et al. Relating chemo-mechanical hysteresis and formation protocols for anode-free lithium metal batteries. *J. Electrochem. Soc.* **171**, 040506 (2024).
130. Liu, Z. et al. Revealing the degradation pathways of layered Li-rich oxide cathodes. *Nat. Nanotechnol.* **19**, 1821–1830 (2024).
131. Li, L. et al. Self-heating-induced healing of lithium dendrites. *Science* **359**, 1513–1516 (2018).
132. Li, Q., Tan, S., Li, L., Lu, Y. & He, Y. Understanding the molecular mechanism of pulse current charging for stable lithium-metal batteries. *Sci. Adv.* **3**, e1701246 (2017).
133. Zhang, Y. et al. Unveiling the impacts of charge/discharge rate on the cycling performance of Li-metal batteries. *ACS Energy Lett.* **10**, 872–880 (2025).
134. Kim, S. et al. Calendar life of lithium metal batteries: accelerated aging and failure analysis. *Energy Storage Mater.* **65**, 103147 (2024).
135. Wood, S. M. et al. Predicting calendar aging in lithium metal secondary batteries: the impacts of solid electrolyte interphase composition and stability. *Adv. Energy Mater.* **8**, 1801427 (2018).
136. Boyle, D. T. et al. Corrosion of lithium metal anodes during calendar ageing and its microscopic origins. *Nat. Energy* **6**, 487–494 (2021).
137. Li, N. et al. Understanding and quantifying capacity loss in storage aging of Ah-level Li metal pouch cells. *InfoMat* **5**, e12402 (2023).
138. Assat, G. & Tarascon, J.-M. Fundamental understanding and practical challenges of anionic redox activity in Li-ion batteries. *Nat. Energy* **3**, 373–386 (2018).
139. Luo, K. et al. Charge-compensation in 3d-transition-metal-oxide intercalation cathodes through the generation of localized electron holes on oxygen. *Nat. Chem.* **8**, 684–691 (2016).
140. Seo, D.-H. et al. The structural and chemical origin of the oxygen redox activity in layered and cation-disordered Li-excess cathode materials. *Nat. Chem.* **8**, 692–697 (2016).
141. Eum, D. et al. Coupling structural evolution and oxygen-redox electrochemistry in layered transition metal oxides. *Nat. Mater.* **21**, 664–672 (2022).
142. Qiu, B. et al. Metastability and reversibility of anionic redox-based cathode for high-energy rechargeable batteries. *Cell Rep. Phys. Sci.* **1**, 100028 (2020).
143. Kang, S., Lee, S., Lee, H. & Kang, Y.-M. Manipulating disorder within cathodes of alkali-ion batteries. *Nat. Rev. Chem.* **8**, 587–604 (2024).
144. Zhang, M. et al. High pressure effect on structural and electrochemical properties of anionic redox-based lithium transition metal oxides. *Matter* **4**, 164–181 (2021).
145. Zuo, W. et al. Li-rich cathodes for rechargeable Li-based batteries: reaction mechanisms and advanced characterization techniques. *Energy Environ. Sci.* **13**, 4450–4497 (2020).
146. Jeong, H.-T. & Kim, W. J. Deformation mechanism maps of pure lithium: their application in determining stack pressure for all-solid-state lithium-ion batteries. *ACS Energy Lett.* **9**, 3237–3251 (2024).
147. Chang, W., Xu, T. & Steingart, D. Chemo-mechanical effects of stack pressure and temperature on anode-free lithium metal batteries. *J. Electrochem. Soc.* **169**, 090530 (2022).
148. Kasnatscheew, J. et al. Determining oxidative stability of battery electrolytes: validity of common electrochemical stability window (ESW) data and alternative strategies. *Phys. Chem. Chem. Phys.* **19**, 16078–16086 (2017).
149. Zhou, M. Y. et al. Quantifying the apparent electron transfer number of electrolyte decomposition reactions in anode-free batteries. *Joule* **6**, 2122–2137 (2022).
150. Gu, Y. et al. Resolving nanostructure and chemistry of solid-electrolyte interphase on lithium anodes by depth-sensitive plasmon-enhanced Raman spectroscopy. *Nat. Commun.* **14**, 3536 (2023).
151. Wang, J. et al. Visualizing and regulating dynamic evolution of interfacial electrolyte configuration during de-solvation process on lithium-metal anode. *Angew. Chem. Int. Ed.* **63**, e202400254 (2024).
152. Glasbeek, M. & Zhang, H. Femtosecond studies of solvation and intramolecular configurational dynamics of fluorophores in liquid solution. *Chem. Rev.* **104**, 1929–1954 (2004).
153. Litman, Y., Chiang, K.-Y., Seki, T., Nagata, Y. & Bonn, M. Surface stratification determines the interfacial water structure of simple electrolyte solutions. *Nat. Chem.* **16**, 644–650 (2024).
154. Yao, N., Chen, X., Fu, Z.-H. & Zhang, Q. Applying classical, ab initio, and machine-learning molecular dynamics simulations to the liquid electrolyte for rechargeable batteries. *Chem. Rev.* **122**, 10970–11021 (2022).
155. Zheng, Z. et al. Quantitatively detecting and characterizing metallic lithium in lithium-based batteries. *Energy Environ. Sci.* **17**, 9051–9092 (2024).
156. Fang, C. C. et al. Quantifying inactive lithium in lithium metal batteries. *Nature* **572**, 511–515 (2019).
This work introduces the concept of chemical titration-based quantification for inactive Li in LMB.
157. Tao, M. M. et al. Quantifying the evolution of inactive Li/lithium hydride and their correlations in rechargeable anode-free Li batteries. *Nano Lett.* **22**, 6775–6781 (2022).
158. Hobold, G. M., Wang, C., Steinberg, K., Li, Y. & Gallant, B. M. High lithium oxide prevalence in the lithium solid–electrolyte interphase for high coulombic efficiency. *Nat. Energy* **9**, 580–591 (2024).
159. Fan, X. & Wang, C. High-voltage liquid electrolytes for Li batteries: progress and perspectives. *Chem. Soc. Rev.* **50**, 10486–10566 (2021).
160. Meng, Y. S., Srinivasan, V. & Xu, K. Designing better electrolytes. *Science* **378**, eabq3750 (2022).
161. Zhang, H. et al. Electrolyte additives for lithium metal anodes and rechargeable lithium metal batteries: progress and perspectives. *Angew. Chem. Int. Ed.* **57**, 15002–15027 (2018).
162. Xia, Y. et al. Designing an asymmetric ether-like lithium salt to enable fast-cycling high-energy lithium metal batteries. *Nat. Energy* **8**, 934–945 (2023).
163. Lu, B. et al. Key parameters in determining the reactivity of lithium metal battery. *ACS Energy Lett.* **8**, 3230–3238 (2023).
164. Puthusseri, D., Parmananda, M., Mukherjee, P. P. & Pol, V. G. Probing the thermal safety of Li metal batteries. *J. Electrochem. Soc.* **167**, 120513 (2020).
165. Jiang, F.-N. et al. Thermal safety of dendritic lithium against non-aqueous electrolyte in pouch-type lithium metal batteries. *J. Energy Chem.* **72**, 158–165 (2022).
166. Zhang, X. et al. Deciphering the thermal failure mechanism of anode-free lithium metal pouch batteries. *Adv. Energy Mater.* **13**, 2203648 (2023).
167. Xu, X. Q. et al. Dendrite-accelerated thermal runaway mechanisms of lithium metal pouch batteries. *SusMat* **2**, 435–444 (2022).
168. Cui, X. et al. Safety hazards of lithium metal batteries: from the perspective of lithium dendrites and thermal runaway. *Energy Fuels* **39**, 7665–7690 (2025).
169. Zhou, Q. et al. A temperature-responsive electrolyte endowing superior safety characteristic of lithium metal batteries. *Adv. Energy Mater.* **10**, 1903441 (2020).
170. Xie, J. & Lu, Y. C. Designing nonflammable liquid electrolytes for safe Li-ion batteries. *Adv. Mater.* **37**, 2312451 (2025).

Acknowledgements

This work is supported by the National Natural Science Foundation of China (22479158, 52272253, 52472266), the External Cooperation Program of Chinese Academy of Sciences (grant no. 181GJHZ2024126MI), the R&D Project of Jiangsu Province (BKBG2024021), Guangdong Basic and Applied Basic Research Foundation (2024A1515011548), Shenzhen Science and Technology Program (KJZD20240903100707011 and JCYJ20240813155846060), the Natural Science Foundation of Ningbo (2024QL041), and the Youth Innovation Promotion Association of Chinese Academy of Sciences (2022299). Y.S.M. acknowledges the support from the University of Chicago international programme.

Author contributions

W.D., B.Q., Y.T., Z.L. and Y.S.M. contemplated the topic and structure of this Review. W.D., B.Q. and Y.S.M. contributed to the writing and editing of all sections of the manuscript. All authors contributed to the discussion of content and edited the manuscript.

Competing interests

The authors declare no competing interests.

Additional information

Peer review information *Nature Reviews Chemistry* thanks Stefan Freunberger, who co-reviewed with Po-Hua Su; Kyu-Young Park; and the other, anonymous, reviewer(s) for their contribution to the peer review of this work.

Related links

Molecular Universe of SES AI: https://www.ses.ai
QuantumScape's FlexFrame: https://www.quantumscape.com/blog/introducing-flexframe/

[1]Ningbo Institute of Materials Technology and Engineering, Chinese Academy of Sciences, Ningbo, People's Republic of China. [2]Advanced Energy Storage Technology Research Center, Shenzhen Institutes of Advanced Technology, Chinese Academy of Sciences, Shenzhen, People's Republic of China. [3]Sunwoda Electric Vehicle Battery Co., Ltd., Shenzhen, People's Republic of China. [4]Pritzker School of Molecular Engineering, University of Chicago, Chicago, IL, USA.